# The structure of the R2T complex reveals a different architecture from the related HSP90 cochaperone R2TP

Alberto Palacios-Abella[1,4], Andrés López-Perrote[2,4], Jasminka Boskovic[2], Sandra Fonseca[3], Cristina Úrbez[1], Vicente Rubio[3], Oscar Llorca[2,*], David Alabadí[1,5,*]

[1]Instituto de Biología Molecular y Celular de Plantas (CSIC-UPV), Ingeniero Fausto Elio s/n, 46022 Valencia, Spain

[2]Spanish National Cancer Research Centre (CNIO), Structural Biology Programme, Melchor Fernández Almagro 3, 28029 Madrid, Spain

[3]Centro Nacional de Biotecnología (CSIC), Darwin 3, Campus de Cantoblanco, 28049 Madrid, Spain

[4]These authors contributed equally

[5]Lead contact

[*]Correspondence: ollorca@cnio.es (O.L.), dalabadi@ibmcp.upv.es (D.A.)

**SUMMARY**

The R2TP complex is a specialized HSP90 cochaperone essential for the maturation of macromolecular complexes such as RNAPII and TORC1. R2TP is formed by a hetero-hexameric ring of AAA-ATPases RuvBL1 and RuvBL2, which interact with RPAP3 and PIH1D1. Several R2TP-like complexes have been described, but these are less well characterized. Here we identified, characterized and determined the cryo-EM structure of R2T from *Arabidopsis thaliana*, which lacks PIH1D1 and is probably the only form of the complex in seed plants. In contrast to R2TP, R2T is organized as two rings of AtRuvBL1-AtRuvBL2a interacting back-to-back, with one AtRPAP3 anchored per ring. AtRPAP3 has no effect on the ATPase activity of AtRuvBL1-AtRuvBL2a and binds with a different stoichiometry than in human R2TP. We show that the interaction of AtRPAP3 with AtRuvBL2a and AtHSP90 occurs via a conserved mechanism. However, the distinct architectures of R2T and R2TP suggest differences in their functions and mechanisms.

## INTRODUCTION

The chaperone HSP90 plays an important role in protein homeostasis in eukaryotes, especially under unfavorable cellular conditions when the activity of proteins and protein complexes is challenged [1]. Not surprisingly, the influence of HSP90 activity is ubiquitous in plants. For instance, HSP90 is necessary to buffer genetic variants that may have potential effects on protein stability or activity in *Arabidopsis* [2] .

HSP90 does not act alone but is supported by numerous cochaperones [1]. One of these cochaperones is the R2TP complex, which provides client specificity to HSP90 in the assembly of various protein complexes in yeast and mammals, e.g. the Box C/D and Box H/ACA small nucleolar ribonucleoproteins or the TOR complex [3]. R2TP stands for Rvb1-Rvb2-Tah1-Pih1, after these proteins were identified as members of an HSP90-interacting complex in yeast [4]. Rvb1 and Rvb2 are AAA+ ATPases with orthologs in animals and plants named RuvB-like 1 (RuvBL1) and RuvBL2 (Figure 1A) [5–8]. Rvb1/RuvBL1 and Rvb2/RuvBL2 share > 40 % identity and have a similar structure [9]. Both proteins have an ATPase domain comprising Walker A and Walker B motifs involved in nucleotide binding and ATP hydrolysis, respectively (Figure 1A) [10,11]. The ATPase core is inserted by the prominent Domain II (DII) with an oligonucleotide/oligosaccharide binding-fold (OB-fold) responsible for protein-protein interactions. Purified Rvb1/RuvBL1 and Rvb2/RuvBL2 form homo-oligomeric hexameric complexes on their own [10,11], but the functional complex in cells is believed to comprise both subunits [12,13]. Accordingly, only the RuvBL1-RuvBL2 complex hydrolyses ATP efficiently[13]. Rvb1/RuvBL1 and Rvb2/RuvBL2 are shared with chromatin remodelers SWR1 and INO80-C [14].

Yeast Tah1 is a small protein (12 KDa) with a TPR domain that interacts with the C-terminal MEEVD of HSP90 [4]. In humans, Tah1 ortholog RPAP3 is a larger protein (75 KDa) containing two TPR domains and a C-terminal domain named RuvBL2-Binding Domain (RBD) [15,16]. The plant RPAP3 ortholog (44 KDa) containing a single TPR domain and the RBD has been identified in sorghum (Figure 1A) [17]. Pih1 and its ortholog in animals PIH1D1 contain a C-terminal CS domain that mediates interaction with Tah1/RPAP3 and an N-terminal PIH domain that interacts with clients[18]. Homologs of Pih1/PIH1D1 are exclusively found in bryophytes within the green lineage [19]. Thus, the R2TP in vascular plants such as *Arabidopsis* would be formed by RuvBL1, RuvBL2 and RPAP3. In fact, this

reduced version of the complex, called R2T, has been identified in humans in addition to the canonical one [19,20].

Cryo-EM analyses have provided structural insights into the 3D organization of Rvb1/RuvBL1-Rvb2/RuvBL2[9–11,21,22] and R2TP complexes[16,23,24]. Recombinant Rvb1/RuvBL1 and Rvb2/RuvBL2 proteins form a hetero-hexameric ring, built by alternating subunits, with the ATPase and DII domains on opposite sides defining an AAA-face containing the ATPase domains and the DII-face. Two hexameric rings interact back-to-back through the DII domains to assemble dodecamers. Yeast, human and *Chaetomium thermophilum* Rvb1/RuvBL1 and Rvb2/RuvBL2 purify as a mix of hexameric and dodecameric complexes which seem to be in equilibrium [22,25,26].

The R2TP complex in humans is organized around a hetero-hexameric ring of RuvBL1/RuvBL2 [26]. The RBD of RPAP3 anchors it to the ATPase face of the RuvBL1-RuvBL2 ring, while its flexible region binds PIH1D1 and HSP90 facilitating client recruitment [16]. Each R2TP can accommodate up to three RPAP3 molecules per ring, one per RuvBL2 subunit [16]. In human R2TP, PIH1D1 interacts with the DII domains and thus hinders the formation of double-ring complexes[16,24]. Although the human R2T complex has been identified *in vivo*, its structure is not known.

The human R2TP is associated with the prefoldin-like complex (PFDLc) to form the R2TP/PFDL [27–30], also known as PAQosome, for particle for arrangement of quaternary structure [3]. The PFDLc consists of PFDN2 and PFDN6 and the PFDL proteins URI1, UXT, PDRG1 and ASDURF. Although the function of PFDLc is not known, it may act as an adaptor to recruit clients into the complex [3]. We have recently found that the PFDLc is present in plants [31].

In this work, we have identified the *Arabidopsis* R2T complex. We found that R2T is associated with PFDLc *in vivo* and mediates HSP90 activity. Furthermore, we determined the 3D structure of the *in vitro* assembled R2T complex by cryo-EM. In contrast to the R2TP, the R2T complex is preferentially organized as a dodecameric double ring of AtRuvBL1-AtRuvBL2a with an AtRPAP3 anchored to the ATPase face of either one or the two rings. The different architectures of the R2T and R2TP suggests that each complex might have functional and mechanistic particularities.

**RESULTS**

**The R2T complex is formed *in vivo* and associates to PFDLc in *Arabidopsis***

The *Arabidopsis* PFD6 is part of both the canonical PFD complex and PFDLc [31,32]. As a first approach to identify additional interactors of PFD6, we performed tandem affinity purification (TAP)-MS with *Arabidopsis* PSB-D cell suspensions [33]. The $GS^{rhino}$ tag was fused to the N-terminus of PFD6 and the fusion protein was expressed in PSB-D cell suspensions. We identified numerous peptides corresponding to all subunits of the PFDL and PFD complexes after performing two purification steps (see STAR METHODS for details; Figure 1B, Table 1, Figure S1 and Table S1), as we expected based on our previous results using TAP- or AP-MS with other subunits as baits [31,32]. None of the subunits of the two complexes appeared non-specific (Table 1, Figure S1 and Table S1). We also identified peptides from other proteins associated with PFDLc in humans [27–29]. These include two paralog subunits of nuclear RNA polymerases, NRPB5A and NRPB5C (Figure S2A), and components of the R2T complex (Table 1): AtRPAP3, AtRuvBL1, and AtRuvBL2a[34]. Although AtRuvBL1 and AtRuvBL2a appeared nonspecifically in various TAPs (Table 1) [33], we considered them as true interactors given their close association with RPAP3 in the R2TP complex in other organisms [16,19,20].

To confirm the presence of the R2T complex *in vivo* and its association with the PFDLc, we performed AP-MS in *Arabidopsis* PSB-D cell suspensions expressing $GS^{rhino}$-AtRPAP3. As a control, we used cell suspensions expressing the unfused $GS^{rhino}$ tagWe identified AtRuvBL1 and AtRuvBL2a as two of the major interactors (see STAR METHODS for details; Table 2 and Table S1). We also identified all subunits of the PFDLc except ASDURF (Table 2 and Table S1). Overall, our results show that R2T is formed in *Arabidopsis* and that it associates with the PFDLc. The limited number of peptides corresponding to the subunits of the two complexes in each other's purifications (Tables 1 and 2) suggests that only a fraction of each complex is associated with the other in the PSB-D cell suspensions.

**Direct protein-protein interactions within the R2T complex**

We confirmed the interactions using yeast two-hybrid (Y2H) assays. We observed interactions between AtRuvBL1 and AtRuvBL2a (Figure 2 and Figure S3) [34], as in other eukaryotes [9]. This is consistent with the high homology between *Arabidopsis* and human orthologs (Figure S4). AtRuvBL2a was able to interact with AtRPAP3, whereas we did not

observe any interaction of the latter with AtRuvBL1 (Figure 2 and Figure S3). This interaction pattern corresponds to that of the human R2TP [16,19]. Although the degree of homology between *Arabidopsis* and human RPAP3 is low (Figure S4), their ability to interact specifically with RuvBL2 is conserved.

We confirmed the interactions by pull-down experiments with recombinant proteins expressed in *E. coli*. We fused a His-tag and the solubility partner IF2DI to the N-terminus of AtRPAP3 and a Strep-tag to its C-terminus. AtRPAP3 was co-expressed with His-AtRuvBL1 and untagged AtRuvBL2a. AtRuvBL1 and AtRuvBL2a co-purified with AtRPAP3 via Strep-tag pull-down, indicating that the three proteins form the R2T complex (Figure 3A). Similarly, sorghum RPAP3 can form a complex with human RuvBL1 and RuvBL2 [17].

**AtRPAP3 does not contribute to the ATPase activity of the R2T complex**

Next, we investigated whether AtRPAP3 has an effect on the ATPase activity of AtRuvBL1-AtRuvBL2a. We purified to homogeneity AtRuvBL1-AtRuvBL2a and AtRPAP3 (Figures S5A and S5B) and then we monitored the ATP consumption by the ATPases in the absence and presence of AtRPAP3 (Figure 3B). An average rate of $9.33 \pm 1.01$ $min^{-1}$ of ATP turnover was calculated for AtRuvBL1-AtRuvBL2a, similar to the human orthologs [35], whereas AtRPAP3 alone did not exert measurable ATP hydrolysis. Addition of AtRPAP3 to AtRuvBL1-AtRuvBL2a did not significantly affect the activity ($8.88 \pm 0.57$ $min^{-1}$ of ATP turnover). Thus, as in humans [20], AtRPAP3 does not regulate AtRuvBL1-AtRuvBL2a ATPase activity.

**Mapping direct protein-protein interactions of R2T with HSP90 and PFDLc**

The TPR domain of AtRPAP3 shows significant homology with human RPAP3 TPR2 that specifically interacts with HSP90 (Figure S4). We found that AtRPAP3 was able to interact with AtHSP90.3, one of the four cytosolic HSP90 isoforms in *Arabidopsis* [36], by Y2H (Figure 2 and Figure S3), suggesting that the role of RPAP3 in the recruitment of HSP90 is conserved in plants.

We next determined which subunits make contacts between the R2T and PFDL complexes. The Y2H analysis showed that AtRuvBL2a interacts with PDRG1, whereas AtRPAP3 does so with PFD2 and PFD6 (Figure 2 and Figure S3). This result shows that

several subunits are involved in establishing contacts between the two complexes, indicating the potential for a close association.

**The R2T complex localizes in both the cytoplasm and the nucleus in *Arabidopsis***

ProteomicsDB [37] analysis of normalized protein levels in *Arabidopsis* organs showed overlapping patterns for AtRPAP3, AtRuvBL1, and AtRuvBL2a, supporting their participation in the same complex (Figure S6A). Next, we determined the subcellular location where the R2T complex is formed. YFP-AtRPAP3 was localized to both the nucleus and cytoplasm in *Nicotiana benthamiana* leaves (Figure 4A and Figure S6B), like in *Arabidopsis* [38]. YFP-AtRuvBL2a showed similar localization *N. bethamiana* leaves, as expected for complex subunits (Figure 4B). To confirm this, we performed Bimolecular Fluorescence Complementation (BiFC) by transient expression of YFN-AtRPAP3 and YFC-AtRuvBL2a in leaves of *N. benthamiana*. We observed the fluorescence of the reconstituted YFP mainly in the cytoplasm, with a weaker signal in the nucleus, while the YFP fluorescence of the negative control pairs was below the detection limit (Figure 4C). These results indicate that AtRPAP3 and AtRuvBL2a can interact at both subcellular locations, likely reflecting the localization of the R2T complex. The weaker nuclear fluorescence in BiFC compared to that of the sole YFP fusions suggests the cytoplasm as the primary, but not exclusive, R2T site, while AtRPAP3 and AtRuvBL2a may have independent nuclear roles. The localization of the R2T complex at both subcellular sites contrasts with R2T in animals, which is assumed to perform nuclear functions due to the preferential localization of the RPAP3-2 isoform in the nucleus [19].

YFP-AtHSP90.3 showed similar subcellular localization to AtRPAP3 and AtRuvBL2a when expressed in leaves of *N. benthamiana* (Figure 4D). Similarly, BiFC analysis showed that the interaction between AtRPAP3 and AtHSP90.3 occurs in the same subcellular localizations as that of AtRPAP3 and AtRuvBL2a (Figure 4E). The BiFC signal was weaker in the nucleus, suggesting that HSP90.3, like AtRPAP3 and AtRuvBL2a, plays an additional role independent of R2T at this site. Overall, these results are consistent the assembly of the R2T complex in plants and that it can function as a cochaperone of HSP90.

**Cryo-EM of the *Arabidopsis* AtRuvBL1-AtRuvBL2a complex**

The lack of an ortholog of PIH1D1 in *Arabidopsis* prompted us to investigate the structure of the R2T complex, which could be potentially different from that of the R2TP [19,20].

We first analyzed the structure of the AtRuvBL1-AtRuvBL2a complex purified to homogeneity using cryo-EM (Figures S5A, S5C and S5D). Images of single molecules of the complex were subjected to image processing (Figure S5C). Most of the reference-free 2D averages resembled those of human RuvBL1-RuvBL2, corresponding to the ring-shaped top views of AtRuvBL1-AtRuvBL2a and the barrel-like side views of dodecameric complexes containing 2 hetero-hexameric rings (Figure S5D). We also found a minor population of side views corresponding to single ring hexameric complexes. Low resolution 3D reconstruction of the dodecameric complex showed two hexameric rings interacting back-to-back through the DII domains (Figure S5E), like what has been observed for human RuvBL1-RuvBL2[39]. The two rings in the complex are flexibly attached, and thus we applied a focused refinement protocol on one of the rings that improved the resolution of the cryo-EM map for this section of the complex to 4.7 Å (Figure S5E). This allowed the fitting of the atomic structure of the human AAA core of the proteins (PDB 2XSZ) [39] into the cryo-EM map, showing a high degree of similarity between the two species at this level of resolution (Figure S5E, bottom panel).

To test the DII domains' role in dodecamer formation, we removed residues 130-236 in AtRuvBL1 and 129-234 in AtRuvBL2a, then expressed and purified the truncated complex AtRuvBL1-ΔDII – AtRuvBL2a-ΔDII (Figure S5F). We investigated its oligomerization state by size exclusion chromatography (SEC) and negative staining EM (Figure S5G). The SEC profile of the AtRuvBL1-AtRuvBL2a complex showed a major peak at an elution volume corresponding to a molecular weight of 660 kDa, according to MW standards, as expected for dodecameric complexes (Figure S5D). The SEC profile of the AtRuvBL1-ΔDII – AtRuvBL2a-ΔDII complex showed a similar peak (660 kDa) and a new major peak around 160 kDa. This suggests that removing the DII domains reduces complex stability, supporting their role in oligomerization. EM analysis of the major SEC peak of the AtRuvBL1-ΔDII – AtRuvBL2a-ΔDII complex revealed larger, undefined particles, suggesting altered oligomerization due to DII domain removal. EM observation of the major SEC peak of the AtRuvBL1-ΔDII – AtRuvBL2a-ΔDII complex revealed larger particles with undefined shapes, suggesting altered oligomerization due removal of the

DII domains. In addition, EM images showed smaller particles that could be intermediate oligomers, compatible with the species eluted at a molecular weight of 160 kDa (Figure S5G). A similar effect was observed in humans, where the truncated proteins assembled smaller oligomers that did not fit into the architecture of hexameric or dodecameric complexes [40]. Overall, the results of the truncated mutants show that the DII domains are required for the assembly of dodecameric species, but also for hexamerization.

**Cryo-EM of the *Arabidopsis* R2T complex**

We purified the R2T complex from *Arabidopsis* in amounts and purity suitable for structural studies (Figure S7A). Cryo-EM and image processing of the *Arabidopsis* R2T complex revealed molecules made of the dodecameric form of the AtRuvBL1-AtRuvBL2a complex (Figure S7B and Table S2). This contrasts with the human R2TP, which consists of a hetero-hexameric RuvBL1-RuvBL2 ring, as PIH1D1, which is not present in *Arabidopsis*, disrupts the interaction between the two RuvBL1-RuvBL2 rings. In addition, some faint densities were observed at the AAA-face of each AtRuvBL1-AtRuvBL2a ring, which we attributed to the C-terminal RBD of AtRPAP3 (Figure S7B, yellow arrows in the right panel). The density of the TPR domain and the flexible region of AtRPAP3 was not visible in the cryo-EM images. We hypothesize that this is due to high flexibility, like the human complex [16].

Whereas AtRuvBL1-AtRuvBL2a contained a mix of single and double-ring complexes (Figure S5D), most molecules detected in R2T were dodecamers (Figure S7B), indicating that this is the major species in the sample (92.5% of particles), while a minor population of hexameric complexes was detected (7.5%). In addition, it should be noted that a small percentage of the images corresponded to top views, which cannot be discerned as belonging to end-views to either type of complex.

In human R2TP, the RuvBL1-RuvBL2 ring is decorated by up to 3 RBDs, one per RuvBL2 subunit. To investigate this in *Arabidopsis* R2T, an image processing workflow designed to characterize the occupancy of the RBDs in each AtRuvBL1-AtRuvBL2a ring was applied to the cryo-EM images (Figure S8). First, we implemented a 3D classification strategy focused on defining the occupancy of one ring. We found that 61.6 % of the particles contained no RBD (free AtRuvBL1-AtRuvBL2a), while 38.4 % contained one (R2T) (Figure S8). Particles containing the RBD were realigned based on the position of

this domain and then the occupancy of the opposite ring was analyzed in a similar manner. After selecting the best quality particles from a 3D classification based on this ring, further processing revealed the co-existence of two populations of R2T complexes. Complex 1 contained one RBD per ring (18% of the particles), while in complex 2 (82% of the particles) only one of the rings was bound to an RBD (Figure 5A and Figure S8). Unexpectedly, the RBD in each ring of complex 1 occupied a defined relative position, and we were unable to find any R2T complex that for a given position of an RDB in one ring would show an alternative position of the RBD in the opposite ring. This is a strong indication of some sort of communication between the two rings in the dodecamer.

**The DII domains are needed for the integrity of R2T dodecamers**

The cryo-EM map of R2T suggested that the DII domains should be required for the stability of the dodecamers. We reconstituted the R2T complex with truncated AtRuvBL1-ΔDII – AtRuvBL2a-ΔDII and performed pull-down experiments (Figure S5H). AtRPAP3 was also able to interact with AtRuvBL1-ΔDII – AtRuvBL2a-ΔDII, indicating that the DII domains are not needed for this interaction, consistent with the R2T structure. However, EM analysis of the mutant R2T complexes showed no dodecamers nor hexamers, with most images and 2D averages difficult to interpret, suggesting intermediate oligomers containing AtRPAP3, AtRuvBL1-ΔDII and AtRuvBL2a-ΔDII (Figure S5H). Overall, our results suggest that truncation of the DII domain not only affects the stability of the dodecameric species, but possibly also that of the hexamers in R2T.

**ATP regulates the conformation and oligomeric state of R2T**

To further study the role of the DII domains in the architecture of R2T, we used CB-6644, a compound that inhibits ATP hydrolysis of human RuvBL1-RuvBL2 [13]. We have recently described that CB-6644 interacts with human RuvBL1-RuvBL2 in the presence of ATP, stabilizing an ATP-bound conformation where the DII domains are in an inward-facing conformation that disrupts dodecameric complexes [41]. We tested the effect of CB-6644 on the ATPase activity of AtRuvBL1-AtRuvBL2a, observing inhibition of ATP hydrolysis (Figure 5B and Figure S5I). Then, we incubated the R2T complex with ATP and CB-6644, and the sample was visualized using EM (Figure 5C). Most dodecameric complexes disassembled into hexamers (Figure 5C)[41]. Interestingly, a similar distribution of

oligomeric species was observed when R2T was incubated only with ATP, suggesting that the nucleotide-saturating experimental conditions were sufficient to observe most of the complexes in the ATP-bound state (Figure 5C).

Altogether, these results support the role of the DII domains in the stability of the dodecameric R2T architecture, but also that this can be affected by changes in the conformation of the DII domains. Moreover, ATP binding and hydrolysis might regulate the transition from dodecamers to hexamers, coupling the oligomeric state of the R2T complex to its ATPase cycle.

**Structure of the AtRuvBL1-AtRuvBL2a-RBD interaction**

To gain insight into the interaction between AtRuvBL1-AtRuvBL2a and AtRPAP3, we conducted a focused 3D refinement on one of the AtRuvBL1-AtRuvBL2a rings containing an RBD to improve resolution. The resolution of the cryo-EM map obtained (3.75 Å) allowed atomic model building for the interaction (Figures 5D and 5E and Figures S9A and S9B). The DII domains were excluded from this analysis because of their flexibility.

The AAA-ring of the R2T complex displays a similar structure to the human R2TP complex [16], with the RBD of AtRPAP3 attached to the AAA-face through the interaction with the AtRuvBL2a subunit (Figures 5A, 5D and 5E). However, we only found 1 RBD per ring compared to human R2TP, although the reconstitution strategy used for each complex was different[16]. The AtRuvBL1 subunits were occupied by ADP and their N-terminal end, containing two conserved histidine residues, contributed to the binding of ADP trapped in the nucleotide binding pocket (Figure 5F). However, all AtRuvBL2a subunits were in an apo state with no bound nucleotide, which correlated with the lack of density for their N-terminus in the cryo-EM map, suggesting that they are disordered (Figure 5F). The N-terminus of RuvBL2 has been described as a gate-keeper segment that controls nucleotide status in several human RuvBL1-RuvBL2-containing complexes [23,35,42].

The atomic structure of AtRPAP3 RBD comprises 8 helical segments ($\alpha$1-$\alpha$8), like the human orthologue (Figures S9C, S9D and S9E). Helix $\alpha$1 of the RBD contacts with the C-terminal region of AtRuvBL1, while helix $\alpha$6 and the loop connecting $\alpha$5-$\alpha$6 interact with a positively charged region of AtRuvBL2a (Figure 6A). Inspection of the interaction surface revealed that AtRPAP3 residues R428 and M431 make contacts with AtRuvBL2a.

It should be noted that these two residues are conserved in humans (Figure S4; green asterisks), where their mutation impairs the interaction between RPAP3 and RuvBL2 [19].

**The mutations R428A and M431A in AtRPAP3 impair the AtRPAP3-AtRuvBL2a interaction *in vivo***

To determine the importance of R428 and M431 for interaction, we changed these two residues to A (Figure 6B), as this change in human RPAP3 prevents interaction with RuvBL2 [19]. The mutant version AtRPAP3mut2 lost the ability to interact with AtRuvBL2a in Y2H (Figure 6C, bottom panel). This was not due to an overall negative impact of the double mutation on AtRPAP3mut2, as it retained the ability to interact with AtHSP90.3 (Figure 6C; see also Figure 7D). Next, we tested the interaction of myc-AtRuvBL2a with the two versions of YFP-AtRPAP3 by co-immunoprecipitation (co-IP) in *N. benthamiana*. The YFP-AtRPAP3 versions were difficult to extract with the co-IP buffer and the signal was below the detection limit in the input lanes but was visible after IP (Figure 6D). myc-AtRuvBL2a was co-immunoprecipitated with anti-GFP antibodies from extracts co-expressing YFP-AtRPAP3 or the unrelated YFP-AtRPAP3mut6 (see below), whereas the interaction was reduced for YFP-AtRPAP3mut2 (Figure 6D). These results confirm that the contacts of AtRPAP3 R428 and M431 with AtRuvBL2a, which we identified in the cryo-EM analysis, are important for the interaction of the two proteins *in planta*.

**The TPR domain of AtRPAP3 mediates the interaction with HSP90**

The conserved MEEVD C-terminal peptide of HSP90 contacts human RPAP3 via the TPR2 domain [43]. We modeled the structure of the TPR domain of AtRPAP3 bound to the MEEVD peptide based on the structure of the peptide bound to human RPAP3 TPR2 [43]. Modeling showed that the AtRPAP3 TPR can adopt a 3D structure like that of human RPAP3 TPR2 (Figure 7A), as shown for sorghum RPAP3 [17]. The six residues of human TPR2 that contact HSP90 [43] are conserved in AtRPAP3 TPR (Figure S4; red asterisks). Modeling showed that the MEEVD peptide also contacts the six residues in *Arabidopsis* TPR (Figure 7A).

We next designed an AtRPAP3 version in which the six residues were changed to A, which we named AtRPAP3mut6 (Figure 7B). As shown in Figure 7C, AtRPAP3mut6 was specifically impaired to interact with AtHSP90.3 in Y2H, while it retained the ability to

interact with AtRuvBL2a (see also Figure 6D). Next, we expressed myc-AtHSP90.3 alone or together with YFP-AtRPAP3, YFP-AtRPAP3mut6 or YFP-AtRPAP3mut2 in leaves of *N. benthamiana*. We could not detect the different AtRPAP3 versions in the input lanes of the immunoblot, but they were detected after IP (Figure 7D). myc-AtHSP90.3 was efficiently immunoprecipitated with anti-GFP antibodies from extracts of leaves co-expressing either YFP-AtRPAP3 or YFP-AtRPAP3mut2, but not from extracts co-expressing AtRPAP3mut6, in which the intensity of the myc-AtHSP90.3 band matched that of the negative control (Figure 7D). These results suggest that *Arabidopsis* RPAP3 interacts with HSP90 via the same mechanism as its orthologs in humans.

**AtRPAP3 is required for the function of HSP90**

We aimed next at determining the importance of AtRPAP3 for HSP90 function in *Arabidopsis*. As proxy to disturb HSP90 we used geldanamycin (GDA), which inhibits the binding of ATP to the chaperone and blocks it in an open state [1,44]. We treated two-day-old WT seedlings and seedlings with the *AtRPAP3* mutant allele *tpr5-2* [38] with mock solution or 10 μM GDA and analyzed the morphological changes after ten days of treatment (Figures 8A and 8B). The growth of the mutant seedlings was less affected by GDA than that of the WT. This result indicates that AtRPAP3 activity is required for HSP90 to fully respond to GDA.

To understand GDA tolerance, we investigated whether the inhibitor affects the interaction between AtRPAP3 and AtHSP90.3 in *Arabidopsis* seedlings. To this end, we expressed a *pAtHSP90.3:6xHis-TEV-3xFLAG-AtHSP90.3* construct in the *AtRPAP3-GFP tpr5-2* background [38]. Seven-day-old seedlings expressing AtRPAP3-GFP or 6xHis-TEV-3xFLAG-AtHSP90.3/AtRPAP3-GFP fusion proteins were treated with mock solution or 20 μM GDA for 24 h and the interaction between both proteins was analyzed by co-IP. Interestingly, AtRPAP3-GFP was more efficiently co-immunoprecipitated by anti-FLAG antibodies from samples treated with GDA (Figure 8C). This is consistent with the observation that in human HEK293T cells, the interaction of HSP90 with RPAP3, PIH1D1 and URI1 is preferentially detected in cells treated with GDA [45]. The R2T may therefore bind AtHSP90 via AtRPAP3 when the chaperone is in an open conformation, helping to ensure that HSP90 reaches a stage in its cycle that makes it ready to bind ATP or

eventually GDA. The reduced activity of AtRPAP3 in the *tpr5-2* mutant likely makes AtHSP90 less susceptible to binding GDA, hence the tolerance shown.

## DISCUSSION

The key feature of the R2T complex found in this work is that its structure is substantially different from that of the related R2TP cochaperone complex. R2T is organized in a double ring of AtRuvBL1-AtRuvBL2a, while the R2TP contains a single ring [16,23,24]. The core of the R2TP and R2T complexes is formed by the Rvb1/RuvBL1-Rvb2/RuvBL2 ATPases, which in isolation assemble into hexameric rings as well as dodecameric complexes. Dodecamers have been found in several species including yeast, human and *Chaetomium thermophilum*, and their structures have been determined using several techniques including cryo-EM and X-ray crystallography [22,25,26]. They were also detected using small-angle X-ray scattering (SAXS) in solution [26]. However, the functional relevance of each type of complex is unclear. In the case of R2TP, the DII-face of the ring in yeast and humans is occupied by Tah1-Pih1 and PIH1D1, respectively, which disrupts the formation of dodecamers, whereas this is not the case for R2T where PIH1D1 is absent [46,47]

The functional role of the dodecameric versus hexameric organization in R2T and R2TP complexes remains unclear. Yeast studies suggest that Rvb1-Rvb2 can switch between these forms during INO80-C assembly [46]. Interaction of the Ino80 subunit with Rvb1-Rvb2 triggers dodecamerization and ATPase activity, leading to ring separation, with one ring binding Ino80. This dodecamer-hexamer cycle depends on client protein insertion, facilitating INO80 complex assembly. The binding of Pih1-Tah1 or PIH1D1 to Rvb1-Rvb2 or anchored RPAP3 may disrupt the dodecamer, promoting the ATPase cycle and client transfer to HSP90 in yeast and humans. Structural analysis of *Arabidopsis* R2T suggests that its rings are flexibly connected via AtRuvBL1-AtRuvBL2a DII domain interactions, potentially enabling client-triggered ATPase activity and ring separation for client transfer to AtHSP90. Without a PIH1D1 homolog, AtRPAP3 may alternatively trigger this process upon client binding. In addition, we have shown here that various subunits of the PFDLc interact directly with AtRuvBL2a and AtRPAP3, so it is conceivable that recruitment of PFDLc contributes to the potential dodecamer-hexamer cycle. It is also likely that a potential cycle between hexamers and dodecamers would be

coordinated not only by the clients but also by ATP binding and hydrolysis. Binding of ATP to human RuvBL1-RuvBL2 complexes induces a large conformational change in the DII domain [41]. In the ATP bound conformation, DII domain cannot hold the dodecameric complexes, and we have observed a similar finding here for R2T. This strongly supports a model where clients and ATP binding/hydrolysis could be coupled to an hexameric/dodecameric cycle.

In addition, the R2T complex is built containing only one RBD per AtRuvbl1-AtRuvBL2a ring. This contrasts with human R2TP, where the hexameric ring harbors 1, 2 or 3 RBDs, one per RuvBL2 subunit [16,23]. If the binding of AtRPAP3 to each AtRuvBL2a subunit were completely independent, one would expect there to be at least a small population of molecules harboring more than one RBD per ring. However, our results are consistent with a model in which binding of the first AtRPAP3 molecule renders further binding events less favorable. Interestingly, R2T complex 1 contains 2 RBD domains, one per ring. If the interaction of AtRPAP3 with each of the rings were completely independent, one would expect that for a given position of the RBD in one of the rings, we would have found more than one possible position for the RBD in the opposite ring, which is not the case. Overall, the structure of R2T suggests the existence of allosteric communication between the AtRuvBL2a molecules within each ring and between the two rings. We cannot exclude the possibility that the different occupancy for RPAP3 between human R2TP and *Arabidopsis* R2T may be due in part to the different methodology used to reconstitute the two complexes. Human R2TP was prepared by mixing an excess of RPAP3 with RuvBL1-RuvBL2, whereas *Arabidopsis* R2T was produced by co-expressing all subunits in cells. In either case, it can be argued that this latter method may better reflect what might happen *in vivo*.

Our results show that AtRPAP3 is required for HSP90 activity, indicating that R2T may act as an allosteric regulator or adaptor in *Arabidopsis*. Like yeast, where the Tah1-Pih1 dimer binds HSP90 and locks it in the open conformation inhibiting ATPase activity [47], AtRPAP3 binds HSP90 in an open state, as shown with the GDA inhibitor. R2TP facilitates client transfer to HSP90 [48], but an independent allosteric regulatory role cannot be ruled out. *Arabidopsis* RPAP3 interactors include known mammalian R2TP-HSP90 clients, such as RNAPII subunits [30], and adaptors such as ZNHIT2 [28,42] and the TTT

complex [49] (Figures S2A and S2B and Table S1), suggesting R2T aids client transfer and potentially modulates chaperone activity.

In *Arabidopsis* and other species, R2T is associated with the loss of Pih1/PIH1D1 ortholog, which is absent in species without cilia [19]. This suggests that the role of the R2TP in cilia formation was key in maintaining the full complex. In the liverwort plant *Marchantia polymorpha*, expression of *Pih1/PIH1D1* homologs is restricted to the male sex organ that produces sperm (Figure S10) [50]. Its restriction to reproductive organs may have driven R2TP specialization. The absence of R2TP in seed plants and outside the male reproductive organs in non-seed plants suggests that its functions have been taken over by R2T. In humans, the R2T is mainly nuclear [19], as the RPAP3-2 isoform is a nuclear protein, whereas AtRPAP3 localizes in both nucleus and cytoplasm, suggesting its localization change likely aided specialization of the R2TP in non-seed plants and persisted after the loss of Pih1/PIH1D1 in seed plants.

## RESOURCE AVAILABILITY

### Lead Contact

Further information and requests for resources and reagents should be directed to and will be fulfilled by the lead contact, David Alabadí (dalabadi@ibmcp.upv.es).

### Materials availability

All unique reagents generated in this study are available from the lead contact upon reasonable request.

### Data and code availability

- The cryo-EM maps and atomic models for AtRuvBL1-AtRuvBL2a and R2T have been deposited in the EM and Protein Data Banks with accession codes EMD-19894 and PDB ID 9EQ2 and are publicly available as of the date of publication. The accession codes are listed in the key resources table.
- This paper does not report original code.
- Any additional information required to reanalyze the data reported in this paper is available from the lead contact upon request.

**ACKNOWLEDGMENTS**

The authors thank Prof. Toru Fujiwara (The University of Tokyo, Tokyo, Japan) for providing seeds of *tpr5-2* and *pAtRPAP3:AtRPAP3-GFP tpr5-2 Arabidopsis* lines, and Johanne Le Coq and Carmen García-Martín for help in EM sample preparation and imaging. This research was funded by grants PID2019-109925GB-I00 and PID2022-141447NB-I00 to D.A. and by grants PID2020-114429RB-I00 and PID2023-146110NB-I00 to O.L. funded by MCIN/AEI/10.13039/501100011033 and by the European Union (EU) Regional Development Fund (ERDF) "A way of making Europe". A.P-A. was supported by a Ministerio de Educación predoctoral contract (FPU17/05186). O.L. laboratory also had the support from the National Institute of Health Carlos III to CNIO. Cryo-EM data used in this work for the structure of R2T was obtained at the Diamond Light Source cryo-EM facility at the UK's National Electron Bio-imaging Center (eBIC) under BAG Proposal No BI26876 "Stop cancer - structural studies of macromolecular complexes involved in cancer by cryo-EM".

**AUTHORS CONTRIBUTIONS**

A.P.-A., A.L.-P., O.L. and D.A. conceived the research and designed the experiments; A.P.-A. and A.L.-P. performed recombinant protein expression, purification and protein complex assembly; A.L.-P. performed biochemical experiments and the preparation of cryo-EM grids; A.L.-P. and J.B. performed image processing and model building. A.P.-A., S.F., C.U., V.R. and D.A. performed the proteomic analyses; A.P.-A performed the experiments in yeast, *Arabidopsis* and *N. benthamiana*; O.L. and D.A wrote the manuscript, and A.P.-A., A.L.-P. and J.B. edited the manuscript. All authors contributed to the manuscript and discussed the results extensively.

**DECLARATION OF INTERESTS**

The authors declare no competing interests.

**STAR METHODS**

Detailed methods are provided in the online version of this paper and include the following:

- KEY RESOURCES TABLE

- EXPERIMENTAL MODEL AND STUDY PARTICIPANT DETAILS
- METHODS DETAILS
    - Preparation of transgenic *Arabidopsis* lines
    - Identification of PFD6 and AtRPAP3 interactors
    - Yeast two-hybrid assays
    - Confocal microscopy
    - Bimolecular fluorescence complementation assay
    - Cloning, expression and purification of recombinant proteins
    - ATPase assays
    - Cryo-EM
    - Image processing
    - Model building
    - Protein co-immunoprecipitation assays
    - Growth assay in response to geldanamycin
- QUANTIFICATION AND STATISTICAL ANALYSIS

**SUPPLEMENTAL INFORMATION**

Document S1. Figures S1-S10 and Tables S2 and S3.

Table S1. Excel file containing data related to Table 1, Table 2, Figure S1 and Figure S2.

**FIGURE LEGENDS**

**Figure 1. Schematic representation of the subunits of the *Arabidopsis* R2T and PFDL complexes.**

(A) Motifs involved in ATP hydrolysis, the DII domain and domains forming the AAA+ core are indicated in AtRuvBL1 and AtRuvBL2a. The AtRPAP3 subunit contains a TPR domain and the RBD at the C-terminus. (B) The PFD/PFDL schematics show the single and the double β-hairpin connecting the two α-helices in the α-type and β-type prefoldins, respectively. For AtURI, the RPB5-interacting domain and the URI box are shown. The α-helices are marked as a helical line above each protein.

**Figure 2. Direct interactions between subunits of R2T and PFDL complexes.**

Diagram showing the results of the Y2H assays of the interactions between the subunits of the R2T and PFDL complexes. See also Figure S3.

**Figure 3. Assembly of R2T in vitro and ATPase activity.**

(A) Interaction pull-down assays. Left panel shows a control experiment of AtRuvBL1-AtRuvBL2a purification using Ni-NTA and StrepTactin XT resins. After extensive washing, proteins were eluted with imidazole in the case of Ni-NTA resin and biotin in the case of StrepTactin XT resin and analyzed by SDS-PAGE and Coomassie staining. Right panel shows the purification of R2T complex from an *E. coli* culture expressing the three subunits using AtRPAP3 as bait with StrepTactin XT resin. AtRuvBL1-AtRuvBL2a were eluted from the StrepTactin XT resin, indicating binding to AtRPAP3. Input (I), last wash fraction prior elution (W), elution 1 (E1) and elution 2 (E2) for both experiments are shown.

(B) ATPase activity assays of AtRuvBL1-AtRuvBL2a in absence and presence of AtRPAP3. Upper panel shows representative time course curves of ATP turn over by AtRuvBL1-AtRuvBL2a (grey line), a control experiment of AtRPAP3 alone (brown) and R2T (purple). Relative ATPase activities are represented in the bottom graph as mean ± S.D. values from three replicates, considering ATP hydrolysis by AtRuvBL1-AtRuvBL2a 100% activity. One-way ANOVA test was used for the comparison of statistical significance. *****: $P < 0.0001$, ns: not significant. See also Figure S5.

**Figure 4. Subcellular localization of AtRPAP3, AtRuvBL2a and AtHSP90.3 in *N. benthamiana* and their interaction.**

(A, B, D) Nuclear and cytoplasmic localization of AtRPAP3, AtRuvBL2a and AtHSP90.3, respectively (scale bar: 10 µm). See also Figures S6 and S11.

(C, E) BiFC assays in leaves of *N. benthamiana*. AtRPAP3 fused to the N-terminal YFP tag (YFN) was co-expressed with AtRuvBL2a (C) and AtHSP90.3 (E) fused to the C-terminal YFP tag (YFC). YFN-AtJAZ3 and YFC-AtBBX24, which do not interact with AtRPAP3, AtRuvBL2a and AtHSP90.3, were used as negative controls. The insets show the fluorescence of a representative nucleus. Bright field images are shown below. Scale bar: 25 µm.

**Figure 5. Architecture of the *Arabidopsis* R2T complex.**

(A) Low resolution structures of the dodecameric R2T complexes. Note that only the RBD domain of AtRPAP3 (in yellow) was visualized due to the flexibility of the TPR and linker regions of the protein. Interaction of the RBD domains was orchestrated in an organized manner in opposite sides of the AtRuvBL1-AtRuvBL2a dodecamer. See also Figures S7, S8, and Table S2.

(B) Relative ATPase activities of AtRuvBL1-AtRuvBL2a in the presence of increasing concentrations of the CB-6644 inhibitor (0, 0.01, 0.1, 1, 10 and 100 μM), represented as mean ± S.D. values from three replicates, considering ATP hydrolysis by AtRuvBL1-AtRuvBL2a in absence of the inhibitor 100% activity. Statistical significance comparison was estimated with One-way ANOVA test. *: P=0.0122, ***: P=0.0002, ****: P<0.0001. See also Figure S5.

(C) Negative staining EM 2D class averages of the R2T complex incubated with ATP (left top panel) or incubated with ATP and the CB-6644 inhibitor (left, bottom panel). Notice that the resolution of the images does not allow for the visualization of the RBD domain of AtRPAP3. Scale bar: 10 nm. The right graph shows the particle distribution for the oligomeric state (hexamer or dodecamer) of each sample derived from the EM experiments. See also Figure S5.

(D) High resolution cryo-EM map of the top ring of R2T complex obtained by focused refinement of the full dodecameric complex. See also Figure S9.

(E) Atomic model for the top hexamer R2T complex. Nucleotide binding pocket of AtRuvBL1 subunits were filled with ADP (red transparent density), while AtRuvBL2a subunits were in an apo-state with no nucleotide bound. See also Figure S9.

(F) Close-up views of the nucleotide binding pockets of AtRuvBL1 (left) and AtRuvBL2a (right). Atomic models of representative subunits are shown highlighting some catalytic residues. Cryo-EM density for the ADP molecule in AtRuvBL1 subunits is shown in red transparency with the atomic model of the nucleotide inside. The nucleotide binding pockets of the AtRuvBL2a subunits were empty and the N-terminal disordered.

**Figure 6. Mutations R428A and M431A in AtRPAP3 impair the AtRPAP3-AtRuvBL2a interaction *in vivo*.**

(A) Atomic model identifying the residues involved in the interaction between AtRuvBL2a and the RBD of AtRPAP3. See also Figures S4, S9, and Table S2.

(B) Schematic of AtRPAP3mut2, a mutant version of AtRPAP3, indicating the amino acid changes in the RBD domain. See also Figure S4.

(C) Y2H assays for the interaction between AtRPAP3 and AtRPAP3mut2, both fused to the GAL4-BD, and AtRuvBL2a and AtHSP90.3, both fused to the GAL4-AD. L, leucine; W, tryptophan; H, histidine. The numbers indicate the dilution used.

(D) Co-immunoprecipitation showing the interaction between AtRPAP3, AtRPAP3mut2 and AtRPAP3mut6 fused to YFP, and AtRuvBL2a fused to a Myc tag in *N. benthamiana*. Total proteins were immunoprecipitated with anti-GFP magnetic beads. The proteins were detected with anti-GFP and anti-Myc antibodies.

**Figure 7. The TPR domain of AtRPAP3 mediates interaction with HSP90.**

(A) Close-up views of the second TPR domain of human RPAP3 and the polar contacts with the C-terminus of HsHSP90α (left) and the TPR domain of AtRPAP3 and the predicted polar contacts with the C-terminus of AtHSP90 (right). See also Figure S4.

(B) Schematic of AtRPAP3mut6, a mutant version of AtRPAP3, indicating the amino acid changes in the TPR domain. See also Figure S4.

(C) Y2H assays for the interaction between AtRPAP3 and AtRPAP3mut6 fused to the GAL4-BD and AtRuvBL2a and AtHSP90.3 fused to the GAL4-AD. L, leucine; W, tryptophan; H, histidine. The numbers indicate the dilution used.

(D) Co-immunoprecipitation showing the interaction between AtRPAP3, AtRPAP3mut2 and AtRPAP3mut6 fused to YFP, and AtHSP90.3 fused to Myc in *N. benthamiana*. Total proteins were immunoprecipitated with anti-GFP magnetic beads from extracts of infiltrated leaves. The proteins were detected with anti-GFP and anti-Myc antibodies.

**Figure 8. AtRPAP3 is required for the function of AtHSP90.**

(A) Fourteen-day-old WT and *trp5-2* seedlings treated with mock solution or with 10 μM GDA.

(B) Total area of 14-day-old seedlings, treated with mock solution or with 10 μM GDA. 33 seedlings per genotype and treatment were measured. Data from one of two

633 replicates are shown. The total area was measured with Biodock. ***, $P < 0.001$; ns, not
634 significant.
635 (C) Co-immunoprecipitation showing the interaction between AtRPAP3-GFP and 6xHis-
636 TEV-3xFLAG-AtHSP90.3 (labeled as 3xFLAG-AtHSP90.3) in *Arabidopsis*. Total proteins
637 were immunoprecipitated with anti-FLAG magnetic beads from extracts of 7-day-old
638 seedlings treated with mock solution or with 20 µM GDA for 24 hours. The proteins were
639 detected with anti-GFP and anti-FLAG antibodies.
640
641 **TABLES**

**Table 1**. **Subunits of the R2T and PFDL complexes identified by TAP-MS using GS$^{rhino}$-PFD6 as bait. See also Figures S1 and S2.**

| | | Peptides[a] | | | |
|---|---|---|---|---|---|
| | **AGI Code** | **R1** | **R2** | **Ranking[b]** | **Bait groups[c]** |
| **PFD6** | AT1G29990 | 669 | 697 | 1 | 0 |
| **PFD2** | AT3G22480 | 437 | 491 | 3 | 0 |
| **AtURI** | AT1G03760 | 141 | 154 | 5 | 0 |
| **UXT** | AT1G26660 | 143 | 109 | 6 | 0 |
| **PDRG1** | AT3G15351 | 48 | 44 | 10 | 0 |
| **ASDURF** | AT1G49245 | 18 | 23 | 15 | 0 |
| **AtRPAP3** | AT1G56440 | 2 | 5 | 25 | 0 |
| **AtRuvBL1** | AT5G22330 | 7 | 8 | - | 13 |
| **AtRuvBL2a** | AT5G67630 | 4 | 10 | - | 13 |

[a]Number of peptides of each protein identified in each replicate (R1-R2).

[b]Ranking refers to the position of each protein in the filtered list of 50 identified proteins, based on the average number of peptides.

[c]Number of bait groups (out of 62) in which the protein appears as non-specific (see STAR METHODS for details).

642

**Table 2. Subunits of the R2T and PFDL complexes identified by AP-MS using GS$^{rhino}$-AtRPAP3 as bait. See also Figure S2.**

| | | GS$^{rhino}$-AtRPAP3 | | | GS$^{rhino}$ | | |
|---|---|---|---|---|---|---|---|
| | | Peptides / PSM[a] | | | Peptides / PSM[a] | | |
| | AGI code | R1 | R2 | R3 | R1 | R2 | Ranking[b] |
| **AtRPAP3** | AT1G56440 | 106 / 628 | 89 / 585 | 69 / 402 | 1 / 1 | 3 / 3 | 1 |
| **AtRuvBL2a** | AT5G67630 | 94 / 560 | 70 / 480 | 53 / 247 | 17 / 35 | 23 / 47 | 2 |
| **AtRuvBL1** | AT5G22330 | 82 / 503 | 67 / 423 | 44 / 145 | 15 / 21 | 19 / 31 | 3 |
| **AtURI** | AT1G03760 | 26 / 47 | 19 / 31 | 17 / 23 | 0 / 0 | 0 / 0 | 9 |
| **PFD2** | AT3G22480 | 8 / 9 | 9 / 16 | 6 / 9 | 0 / 0 | 0 / 0 | 43 |
| **PDRG1** | AT3G15351 | 4 / 4 | 4 / 6 | 2 / 4 | 0 / 0 | 0 / 0 | 145 |
| **UXT** | AT1G26660 | 5 / 6 | 1 / 2 | 0 / 0 | 0 / 0 | 0 / 0 | 206 |
| **PFD6** | AT1G29990 | 0 / 0 | 2 / 2 | 4 / 4 | 0 / 0 | 0 / 0 | 215 |
| **ASDURF** | AT1G49245 | 0 / 0 | 0 / 0 | 0 / 0 | 0 / 0 | 0 / 0 | - |

[a]Number of peptides/peptide spectrum matches (PSM) of each protein identified in each replicate (R).

[b]Ranking refers to the position of each protein in the filtered list of 223 identified proteins, based on the average number of peptides.

643

644 **REFERENCES**

1. Schopf, F.H., Biebl, M.M., and Buchner, J. (2017). The HSP90 chaperone machinery. Nat Rev Mol Cell Biol *18*, 345–360. https://doi.org/10.1038/nrm.2017.20.
2. Queitsch, C., Sangster, T.A., and Lindquist, S. (2002). Hsp90 as a capacitor of phenotypic variation. Nature *417*, 618–624. https://doi.org/10.1038/nature749.
3. Houry, W.A., Bertrand, E., and Coulombe, B. (2018). The PAQosome, an R2TP-based chaperone for quaternary structure formation. Trends Biochem Sci *43*, 4–9. https://doi.org/10.1016/j.tibs.2017.11.001.
4. Zhao, R., Davey, M., Hsu, Y.C., Kaplanek, P., Tong, A., Parsons, A.B., Krogan, N., Cagney, G., Mai, D., Greenblatt, J., et al. (2005). Navigating the chaperone network: An integrative map of physical and genetic interactions mediated by the hsp90 chaperone. Cell *120*, 715–727. https://doi.org/10.1016/j.cell.2004.12.024.
5. Nano, N., and Houry, W.A. (2013). Chaperone-like activity of the AAA+ proteins RVb1 and RVb2 in the assembly of various complexes. Philosophical Transactions of the Royal Society B: Biological Sciences *368*, 20110399. https://doi.org/10.1098/rstb.2011.0399.
6. Kanemaki, M., Makino, Y., Yoshida, T., Kishimoto, T., Koga, A., Yamamoto, K., Yamamoto, M., Moncollin, V., Egly, J.-M., Muramatsu, M., et al. (1997). Molecular Cloning of a Rat 49-kDa TBP-Interacting Protein (TIP49) That Is Highly Homologous to the Bacterial RuvB. Biochem Biophys Res Commun *235*, 64–68.
7. Majerska, J., Schrumpfova, P.P., Dokladal, L., Schorova, S., Stejskal, K., Oboril, M., Honys, D., Kozakova, L., Polanska, P.S., and Sykorova, E. (2017). Tandem affinity purification of AtTERT reveals putative interaction partners of plant telomerase in vivo. Protoplasma *254*, 1547–1562. https://doi.org/10.1007/s00709-016-1042-3.
8. Holt III, B.F., Boyes, D.C., Ellerströ, M., Siefers, N., Wiig, A., Kauffman, S., Grant, M.R., and Dangl, J.L. (2002). An Evolutionarily Conserved Mediator of Plant Disease Resistance Gene Function Is Required for Normal Arabidopsis Development. Dev Cell *2*, 807–817.
9. Dauden, M.I., López-Perrote, A., and Llorca, O. (2021). RUVBL1–RUVBL2 AAA-ATPase: a versatile scaffold for multiple complexes and functions. Curr Opin Struct Biol *67*, 78–85. https://doi.org/10.1016/j.sbi.2020.08.010.
10. Silva, S.T.N., Brito, J.A., Arranz, R., Sorzano, C.Ó.S., Ebel, C., Doutch, J., Tully, M.D., Carazo, J.M., Carrascosa, J.L., Matias, P.M., et al. (2018). X-ray structure of full-length human RuvB-Like 2 – mechanistic insights into coupling between ATP binding and mechanical action. Sci Rep *8*. https://doi.org/10.1038/s41598-018-31997-z.
11. Matias, P.M., Gorynia, S., Donner, P., and Carrondo, M.A. (2006). Crystal structure of the human AAA+ protein RuvBL1. Journal of Biological Chemistry *281*, 38918–38929. https://doi.org/10.1074/jbc.M605625200.
12. Izumi, N., Yamashita, A., Iwamatsu, A., Kurata, R., Nakamura, H., Saari, B., Hirano, H., Anderson, P., and Ohno, S. (2010). AAA+ proteins RUVBL1 and RUVBL2 coordinate PIKK activity and function in nonsense-mediated mRNA decay. Sci Signal *3*, 1–14. https://doi.org/10.1126/scisignal.2000468.
13. Assimon, V.A., Tang, Y., Vargas, J.D., Lee, G.J., Wu, Y., Lou, K., Yao, B., Menon, M.-K., Pios, A., Perez, K.C., et al. (2019). CB-6644 Is a Selective Inhibitor of the

RUVBL1/2 Complex with Anticancer Activity. ACS Chem. Biol *14*, 39. https://doi.org/10.1021/acschembio.8b00904.

14. Candela-Ferré, J., Diego-Martín, B., Pérez-Alemany, J., and Gallego-Bartolomé, J. (2024). Mind The Gap: Epigenetic Regulation Of Chromatin Accessibility In Plants. Plant Physiol. https://doi.org/10.1093/plphys/kiae024.
15. Jeronimo, C., Forget, D., Bouchard, A., Li, Q., Chua, G., Poitras, C., Therien, C., Bergeron, D., Bourassa, S., Greenblatt, J., et al. (2007). Systematic analysis of the protein interaction network for the human transcription machinery reveals the identity of the 7SK capping enzyme. Mol Cell *27*, 262–274. https://doi.org/10.1016/j.molcel.2007.06.027.
16. Martino, F., Pal, M., Munoz-Hernandez, H., Rodriguez, C.F., Nunez-Ramirez, R., Gil-Carton, D., Degliesposti, G., Skehel, J.M., Roe, S.M., Prodromou, C., et al. (2018). RPAP3 provides a flexible scaffold for coupling HSP90 to the human R2TP co-chaperone complex. Nat Commun *9*, 3063. https://doi.org/10.1038/s41467-018-05546-1.
17. Machado Antonio, L., Henrique Martins, G., Zambon Barbosa Aragão, A., Galdi Quel, N., Zazeri, G., Houry, W.A., and Henrique Inacio Ramos, C. (2023). Unveiling the Role of Sorghum RPAP3 in the Function of R2TP Complex: Insights into Protein Assembly in Plants. Plants *12*, 2925. https://doi.org/10.3390/plants12162925.
18. Horejsi, Z., Stach, L., Flower, T.G., Joshi, D., Flynn, H., Skehel, J.M., O'Reilly, N.J., Ogrodowicz, R.W., Smerdon, S.J., and Boulton, S.J. (2014). Phosphorylation-dependent PIH1D1 interactions define substrate specificity of the R2TP cochaperone complex. Cell Rep *7*, 19–26. https://doi.org/10.1016/j.celrep.2014.03.013.
19. Maurizy, C., Quinternet, M., Abel, Y., Verheggen, C., Santo, P.E., Bourguet, M., A, C.F.P., Bragantini, B., Chagot, M.E., Robert, M.C., et al. (2018). The RPAP3-C terminal domain identifies R2TP-like quaternary chaperones. Nat Commun *9*, 2093. https://doi.org/10.1038/s41467-018-04431-1.
20. Seraphim, T. V, Nano, N., Cheung, Y.W.S., Aluksanasuwan, S., Colleti, C., Mao, Y.-Q., Bhandari, V., Young, G., Höll, L., Phanse, S., et al. (2022). Assembly principles of the human R2TP chaperone complex reveal the presence of R2T and R2P complexes. Structure *30*, 1–16. https://doi.org/10.1016/j.str.2021.08.002.
21. Ewens, C.A., Su, M., Zhao, L., Nano, N., Houry, W.A., and Southworth, D.R. (2016). Architecture and Nucleotide-Dependent Conformational Changes of the Rvb1-Rvb2 AAA+ Complex Revealed by Cryoelectron Microscopy. Structure *24*, 657–666. https://doi.org/10.1016/j.str.2016.03.018.
22. López-Perrote, A., Muñoz-Hernández, H., Gil, D., and Llorca, O. (2012). Conformational transitions regulate the exposure of a DNA-binding domain in the RuvBL1-RuvBL2 complex. Nucleic Acids Res *40*, 11086–11099. https://doi.org/10.1093/nar/gks871.
23. Muñoz-Hernández, H., Pal, M., Rodríguez, C.F., Fernández-Leiro, R., Prodromou, C., Pearl, L.H., and Llorca, O. (2019). Structural mechanism for regulation of the AAA-ATPases RUVBL1-RUVBL2 in the R2TP co-chaperone revealed by cryo-EM. Sci Adv *5*, eaaw1616. https://doi.org/10.1126/sciadv.aaw1616.
24. Rivera-Calzada, A., Pal, M., Munoz-Hernandez, H., Luque-Ortega, J.R., Gil-Carton, D., Degliesposti, G., Skehel, J.M., Prodromou, C., Pearl, L.H., and Llorca, O.

(2017). The Structure of the R2TP Complex Defines a Platform for Recruiting Diverse Client Proteins to the HSP90 Molecular Chaperone System. Structure *25*, 1145-1152 e4. https://doi.org/10.1016/j.str.2017.05.016.

25. Jeganathan, A., Leong, V., Zhao, L., Huen, J., Nano, N., Houry, W.A., and Ortega, J. (2015). Yeast Rvb1 and Rvb2 proteins oligomerize as a conformationally variable dodecamer with low frequency. J Mol Biol *427*, 1875–1886. https://doi.org/10.1016/j.jmb.2015.01.010.
26. Lakomek, K., Stoehr, G., Tosi, A., Schmailzl, M., and Hopfner, K.P. (2015). Structural basis for dodecameric assembly states and conformational plasticity of the full-length AAA+ at pases rvb1·Rvb2. Structure *23*, 483–495. https://doi.org/10.1016/j.str.2014.12.015.
27. Cloutier, P., Poitras, C., Faubert, D., Bouchard, A., Blanchette, M., Gauthier, M.S., and Coulombe, B. (2020). Upstream ORF-Encoded ASDURF Is a Novel Prefoldin-like Subunit of the PAQosome. J Proteome Res *19*, 18–27. https://doi.org/10.1021/acs.jproteome.9b00599.
28. Cloutier, P., Poitras, C., Durand, M., Hekmat, O., Fiola-Masson, E., Bouchard, A., Faubert, D., Chabot, B., Coulombe, B., Fiola-Masson, É., et al. (2017). R2TP/Prefoldin-like component RUVBL1/RUVBL2 directly interacts with ZNHIT2 to regulate assembly of U5 small nuclear ribonucleoprotein. Nat Commun *8*, 15615. https://doi.org/10.1038/ncomms15615.
29. Cloutier, P., Al-Khoury, R., Lavallee-Adam, M., Faubert, D., Jiang, H., Poitras, C., Bouchard, A., Forget, D., Blanchette, M., Coulombe, B., et al. (2009). High-resolution mapping of the protein interaction network for the human transcription machinery and affinity purification of RNA polymerase II-associated complexes. Methods *48*, 381–386. https://doi.org/10.1016/j.ymeth.2009.05.005.
30. Boulon, S., Pradet-Balade, B., Verheggen, C., Molle, D., Boireau, S., Georgieva, M., Azzag, K., Robert, M., Ahmad, Y., Neel, H., et al. (2010). HSP90 and its R2TP/Prefoldin-like cochaperone are involved in the cytoplasmic assembly of RNA polymerase II. Mol Cell *39*, 912–924. https://doi.org/10.1016/j.molcel.2010.08.023.
31. Gómez-Mínguez, Y., Palacios-Abella, A., Costigliolo-Rojas, C., Barber, M., Hernández-Villa, L., Úrbez, C., and Alabadí, D. (2024). The prefoldin-like protein AtURI exhibits characteristics of intrinsically disordered proteins. FEBS Lett *598*, 556–570. https://doi.org/10.1002/1873-3468.14811.
32. Blanco-Touriñán, N., Esteve-Bruna, D., Serrano-Mislata, A., Esquinas-Ariza, R.M., Resentini, F., Forment, J., Carrasco-López, C., Novella-Rausell, C., Palacios-Abella, A., Carrasco, P., et al. (2021). A genetic approach reveals different modes of action of prefoldins. Plant Physiol *187*, 1534–1550. https://doi.org/10.1093/plphys/kiab348.
33. Van Leene, J., Eeckhout, D., Cannoot, B., De Winne, N., Persiau, G., Van De Slijke, E., Vercruysse, L., Dedecker, M., Verkest, A., Vandepoele, K., et al. (2015). An improved toolbox to unravel the plant cellular machinery by tandem affinity purification of Arabidopsis protein complexes. Nat Protoc *10*, 169–187. https://doi.org/10.1038/nprot.2014.199.
34. Schorova, S., Fajkus, J., Zaveska Drabkova, L., Honys, D., and Schrumpfova, P.P. (2019). The plant Pontin and Reptin homologues, RuvBL1 and RuvBL2a,

colocalize with TERT and TRB proteins in vivo, and participate in telomerase biogenesis. Plant J *98*, 195–212. https://doi.org/10.1111/tpj.14306.

35. López-Perrote, A., Hug, N., González-Corpas, A., Rodríguez, C.F., Serna, M., García-Martín, C., Boskovic, J., Fernandez-Leiro, R., Caceres, J.F., and Llorca, O. (2020). Regulation of RUVBL1-RUVBL2 AAA-ATPases by the nonsense-mediated mRNA decay factor DHX34, as evidenced by Cryo-EM. Elife *9*, e63049. https://doi.org/10.1101/2020.09.28.317487.
36. Krishna, P., and Gloor, G. (2001). The Hsp90 family of proteins in Arabidopsis thaliana. Cell Stress Chaperones *6*, 238–246.
37. Samaras, P., Schmidt, T., Frejno, M., Gessulat, S., Reinecke, M., Jarzab, A., Zecha, J., Mergner, J., Giansanti, P., Ehrlich, H.C., et al. (2020). ProteomicsDB: A multi-omics and multi-organism resource for life science research. Nucleic Acids Res *48*, D1153–D1163. https://doi.org/10.1093/nar/gkz974.
38. Sotta, N., Shantikumar, L., Sakamoto, T., Matsunaga, S., and Fujiwara, T. (2016). TPR5 is involved in directional cell division and is essential for the maintenance of meristem cell organization in Arabidopsis thaliana. J Exp Bot *67*, 2401–2411. https://doi.org/10.1093/jxb/erw043.
39. Gorynia, S., Bandeiras, T.M., Pinho, F.G., McVey, C.E., Vonrhein, C., Round, A., Svergun, D.I., Donner, P., Matias, P.M., and Carrondo, M.A. (2011). Structural and functional insights into a dodecameric molecular machine - The RuvBL1/RuvBL2 complex. J Struct Biol *176*, 279–291. https://doi.org/10.1016/j.jsb.2011.09.001.
40. Niewiarowski, A., Bradley, A.S., Gor, J., McKay, A.R., Perkins, S.J., and Tsaneva, I.R. (2010). Oligomeric assembly and interactions within the human RuvB-like RuvBL1 and RuvBL2 complexes. Biochemical Journal *429*, 113–125. https://doi.org/10.1042/BJ20100489.
41. García-Martín, C., López-Perrote, A., Boskovic, J., and Llorca, O. (2024). Mechanism of allosteric inhibition of RUVBL1-RUVBL2 ATPase by the small molecule CB-6644. Cell Rep Phys Sci *5*. https://doi.org/10.1016/j.xcrp.2024.101982.
42. Serna, M., Gonz, A., Degliesposti, G., Zarzuela, E., Skehel, J.M., and Mu, J. (2021). CryoEM of RUVBL1 – RUVBL2 – ZNHIT2, a complex that interacts with pre-mRNA-processing-splicing factor 8. Nucleic Acids Res *50*, 1128–1146.
43. Henri, J., Chagot, M.E., Bourguet, M., Abel, Y., Terral, G., Maurizy, C., Aigueperse, C., Georgescauld, F., Vandermoere, F., Saint-Fort, R., et al. (2018). Deep Structural Analysis of RPAP3 and PIH1D1, Two Components of the HSP90 Co-chaperone R2TP Complex. Structure *26*, 1196–1209. https://doi.org/10.1016/j.str.2018.06.002.
44. Roe, S.M., Prodromou, C., O'Brien, R., Ladbury, J.E., Piper, P.W., and Pearl, L.H. (1999). Structural basis for inhibition of the Hsp90 molecular chaperone by the antitumor antibiotics radicicol and geldanamycin. J Med Chem *42*, 260–266. https://doi.org/10.1021/jm980403y.
45. Gano, J.J., and Simon, J.A. (2010). A proteomic investigation of ligand-dependent HSP90 complexes reveals CHORDC1 as a novel ADP-dependent HSP90-interacting protein. Mol Cell Proteomics *9*, 255–270. https://doi.org/10.1074/mcp.M900261-MCP200.

46. Zhou, C.Y., Stoddard, C.I., Johnston, J.B., Trnka, M.J., Echeverria, I., Palovcak, E., Sali, A., Burlingame, A.L., Cheng, Y., and Narlikar, G.J. (2017). Regulation of Rvb1/Rvb2 by a Domain within the INO80 Chromatin Remodeling Complex Implicates the Yeast Rvbs as Protein Assembly Chaperones. Cell Rep *19*, 2033–2044. https://doi.org/10.1016/j.celrep.2017.05.029.
47. Eckert, K., Saliou, J.M., Monlezun, L., Vigouroux, A., Atmane, N., Caillat, C., Quevillon-Chéruel, S., Madiona, K., Nicaise, M., Lazereg, S., et al. (2010). The Pih1-Tah1 cochaperone complex inhibits Hsp90 molecular chaperone ATPase activity. Journal of Biological Chemistry *285*, 31304–31312. https://doi.org/10.1074/jbc.M110.138263.
48. Lynham, J., and Houry, W.A. (2022). The Role of Hsp90-R2TP in Macromolecular Complex Assembly and Stabilization. Biomolecules *12*, 1045. https://doi.org/10.3390/biom12081045.
49. Toullec, D., Elias-Villalobos, A., Faux, C., Lledo, G., Sevéno, M., and Helmlinger, D. (2021). The Hsp90 Cochaperone TTT Promotes Cotranslational Maturation of PIKK Kinases Prior to Complex Assembly. Cell Rep *37*, 109867. https://doi.org/10.2139/ssrn.3742245.
50. Bowman, J.L., Kohchi, T., Yamato, K.T., Jenkins, J., Shu, S., Ishizaki, K., Yamaoka, S., Nishihama, R., Nakamura, Y., Berger, F., et al. (2017). Insights into Land Plant Evolution Garnered from the Marchantia polymorpha Genome. Cell *171*, 287-304 e15. https://doi.org/10.1016/j.cell.2017.09.030.
51. Koncz, C., and Schell, J. (1986). The promoter of TL-DNA gene 5 controls the tissue-specific expression of chimaeric genes carried by a novel type of Agrobacterium binary vector. Mol Gen Genet *204*, 383–396. https://doi.org/10.1007/BF00331014.
52. Belda-Palazón, B., Ruiz, L., Martí, E., Tárraga, S., Tiburcio, A.F., Culiáñez, F., Farràs, R., Carrasco, P., and Ferrando, A. (2012). Aminopropyltransferases Involved in Polyamine Biosynthesis Localize Preferentially in the Nucleus of Plant Cells. PLoS One *7*. https://doi.org/10.1371/journal.pone.0046907.
53. Earley, K.W., Haag, J.R., Pontes, O., Opper, K., Juehne, T., Song, K., and Pikaard, C.S. (2006). Gateway-compatible vectors for plant functional genomics and proteomics. Plant J *45*, 616–629. https://doi.org/TPJ2617 [pii] 10.1111/j.1365-313X.2005.02617.x.
54. Zivanov, J., Nakane, T., Forsberg, B.O., Kimanius, D., Hagen, W.J., Lindahl, E., and Scheres, S.H. (2018). New tools for automated high-resolution cryo-EM structure determination in RELION-3. Elife *7*, e42166. https://doi.org/10.7554/eLife.42166.001.
55. Punjani, A., Rubinstein, J.L., Fleet, D.J., and Brubaker, M.A. (2017). CryoSPARC: Algorithms for rapid unsupervised cryo-EM structure determination. Nat Methods *14*, 290–296. https://doi.org/10.1038/nmeth.4169.
56. Pettersen, E.F., Goddard, T.D., Huang, C.C., Couch, G.S., Greenblatt, D.M., Meng, E.C., and Ferrin, T.E. (2004). UCSF Chimera—A visualization system for exploratory research and analysis. J Comput Chem *25*, 1605–1612. https://doi.org/10.1002/jcc.20084.
57. Croll, T.I. (2018). ISOLDE: A physically realistic environment for model building into low-resolution electron-density maps. Acta Crystallogr D Struct Biol *74*, 519–530. https://doi.org/10.1107/S2059798318002425.

58. Emsley, P., Lohkamp, B., Scott, W.G., and Cowtan, K. (2010). Features and development of Coot. Acta Crystallogr D Biol Crystallogr *66*, 486–501. https://doi.org/10.1107/S0907444910007493.
59. Curtis, M.D., and Grossniklaus, U. (2003). A gateway cloning vector set for high-throughput functional analysis of genes in planta. Plant Physiol *133*, 462–469. https://doi.org/10.1104/pp.103.027979.
60. Esteve-Bruna, D., Carrasco-López, C., Blanco-Touriñán, N., Iserte, J., Calleja-Cabrera, J., Perea-Resa, C., Úrbez, C., Carrasco, P., Yanovsky, M.J., Blázquez, M.A., et al. (2020). Prefoldins contribute to maintaining the levels of the spliceosome LSM2-8 complex through Hsp90 in Arabidopsis. Nucleic Acids Res *48*, 6280–6293. https://doi.org/10.1093/nar/gkaa354.
61. Antosz, W., Pfab, A., Ehrnsberger, H.F., Holzinger, P., Kollen, K., Mortensen, S.A., Bruckmann, A., Schubert, T., Langst, G., Griesenbeck, J., et al. (2017). The Composition of the Arabidopsis RNA Polymerase II Transcript Elongation Complex Reveals the Interplay between Elongation and mRNA Processing Factors. Plant Cell *29*, 854–870. https://doi.org/10.1105/tpc.16.00735.
62. Belda-Palazón, B., Ruíz, L., Martí, E., Tárraga, S., Tiburcio, A.F., Culiáñez, F., Farràs, R., Carrasco, P., and Ferrando, A. (2012). Aminopropyltransferases involved in polyamine biosynthesis localize preferentially in the nucleus of plant cells. PLoS One *7*, e46907. https://doi.org/10.1371/journal.pone.0046907 PONE-D-12-14867 [pii].
63. García-Nafría, J., Watson, J.F., and Greger, I.H. (2016). IVA cloning: A single-tube universal cloning system exploiting bacterial In Vivo Assembly. Sci Rep *6*, 27459. https://doi.org/10.1038/srep27459.
64. Zheng, S.Q., Palovcak, E., Armache, J.P., Verba, K.A., Cheng, Y., and Agard, D.A. (2017). MotionCor2: Anisotropic correction of beam-induced motion for improved cryo-electron microscopy. Nat Methods *14*, 331–332. https://doi.org/10.1038/nmeth.4193.
65. Zhang, K. (2016). Gctf: Real-time CTF determination and correction. J Struct Biol *193*, 1–12. https://doi.org/10.1016/j.jsb.2015.11.003.
66. Yang, Z., Zeng, X., Zhao, Y., and Chen, R. (2023). AlphaFold2 and its applications in the fields of biology and medicine. Signal Transduct Target Ther *8*, 115. https://doi.org/10.1038/s41392-023-01381-z.
67. Afonine, P. V., Poon, B.K., Read, R.J., Sobolev, O. V., Terwilliger, T.C., Urzhumtsev, A., and Adams, P.D. (2018). Real-space refinement in PHENIX for cryo-EM and crystallography. Acta Crystallogr D Struct Biol *74*, 531–544. https://doi.org/10.1107/S2059798318006551.
68. Webb, B., and Sali, A. (2016). Comparative protein structure modeling using MODELLER. Curr Protoc Bioinformatics *2016*, 5.6.1-5.6.37. https://doi.org/10.1002/cpbi.3.

## STAR METHODS

### KEY RESOURCES TABLE

| REAGENT or RESOURCE | SOURCE | IDENTIFIER |
|---|---|---|
| Antibodies | | |
| anti-GFP (JL-8) | Clontech | Cat#-632380 |

| | | |
|---|---|---|
| anti-FLAG-HRP | Sigma-Aldrich | Cat#-H7425 |
| anti-Myc-HRP | Thermo Fisher Sci | Cat#-MA1-81357 |
| anti-Mouse-HRP | Agrisera | Cat#-AS11 1772 |
| IgG from rabbit serum | Sigma-Aldrich | Cat#-I5006 |
| Bacterial and virus strains | | |
| *Escherichia coli* TOP10 | Widely distributed | N/A |
| *Escherichia coli* LOBSTR-BL21(DE3)-RIL | Kerafast | Cat#-EC1002 |
| *Escherichia coli* BL21 (DE3) | Widely distributed | N/A |
| *Agrobacterium tumefaciens* GV3101 (pMP90 C58) | Koncz and Schell[51] | N/A |
| Chemicals, peptides, and recombinant proteins | | |
| PMSF | Sigma-Aldrich | Cat#-52332 |
| cOmplete® EDTA-free protease Inhibitor Cocktail | Roche | Cat#-11836170001 |
| Benzonase Nuclease | Millipore | Cat#-70746 |
| Lysozyme from chicken egg white | Sigma-Aldrich | Cat#-62971 |
| Isopropyl-β-D-1-thiogalactopyranoside (IPTG) | Neo Biotech | Cat#-NB-45-00030 |
| BcMag Epoxy-Activated Magnetic Beads | Bioclone | Cat#-FC101 |
| ChromoTek GFP-Trap® Agarose | Proteintech | Cat#-gta |
| Anti-FLAG M2 Magnetic beads | Sigma-Aldrich | Cat#-M8823 |
| Adenosine 5’-triphosphate (ATP) disodium salt hydrate | Sigma-Aldrich | Cat#-A7699 |
| CB-6644 | MedChem | Cat#-HY-114429 |
| HisTrap HP | Cytiva | Cat#-17524701 |
| StrepTactin®XT 4Flow | IBA Life Sciences | Cat#-2-5013-001 |
| Biotin | IBA Life Sciences | Cat#-2-1016-005 |
| Pyruvate kinase/Lactic dehydrogenase enzymes from rabbit muscle | Sigma-Aldrich | Cat#-P0294 |
| ß-Nicotinamide adenine dinucleotide reduced disodium salt hydrate (NADH) | Sigma-Aldrich | Cat#-N8129 |
| Phospho(enol)pyruvic acid trisodium salt hydrate (PEP) | Sigma-Aldrich | Cat#-P7002 |
| Geldanamycin | MedChem | Cat#-HY-15230 |
| Critical commercial assays | | |
| Gateway™ LR Clonase™ Enzyme mix | Thermo Fisher Sci | Cat#-11791019 |
| SuperSignalTM West Femto | Thermo Fisher Sci | Cat#-34095 |
| Deposited data | | |
| Cryo-EM map of the R2T complex | This paper | EMDB: EMD-19894 |
| Model of the R2T complex | This paper | PDB: 9EQ2 |
| Experimental models: Cell lines | | |
| Arabidopsis PSB-D cell suspension | Van Leene et al.[33] | N/A |
| Experimental models: Organisms/strains | | |
| *Sachcharomyces cerevisiae:* Y187 | Takara | Cat#-630457 |
| *Sachcharomyces cerevisiae:* Y2HGold | Takara | Cat#-630498 |
| *Arabidopsis: tpr5-2* | Sotta et al. [38] | N/A |

| | | |
|---|---|---|
| *Arabidopsis:* AtRPAP3-GFP | Sotta et al. [38] | N/A |
| *Arabidopsis:* 6xHis-TEV-3xFLAG-AtHSP90.3 | This paper | N/A |
| *Arabidopsis:* 6xHis-TEV-3xFLAG-AtHSP90.3/AtRPAP3-GFP | This paper | N/A |
| *Nicotiana benthamiana* lab strain | Widely distributed | N/A |
| Oligonucleotides | | |
| All oligonucleotides are listed in Table S3 | This paper | N/A |
| Recombinant DNA | | |
| pENTR223-AtRPAP3 | ABRC | G67297 |
| pENTR223-AtRuvBL1 | ABRC | GC105109 |
| pENTR223-AURI | ABRC | G51229 |
| pENTR223-UXT | ABRC | G11549 |
| pENTR223-PDRG1 | ABRC | G69205 |
| pENTR223-PFD2 | ABRC | G09515 |
| pENTR223-PFD6 | ABRC | G82091 |
| pENTR223-AtRPAP3mut2 | This paper | N/A |
| pENTR223-AtRPAP3mut6 | This paper | N/A |
| pENTR207-AtHSP90.3 | This paper | N/A |
| pENTR207-AtRuvBL2a | This paper | N/A |
| pENTR207-ASDURF | This paper | N/A |
| pKGNS_rhino | Van Leene et al.[33] | N/A |
| pKGNS_rhino-PFD6 | This paper | N/A |
| pKGNS_rhino-AtRPAP3 | This paper | N/A |
| pMDC43-YFN | Belda-Palazón et al.[52] | N/A |
| pMDC43-YFC | Belda-Palazón et al.[52] | N/A |
| pMDC43-YFN-AtRPAP3 | This paper | N/A |
| pMDC43-YFC-AtRuvBL2a | This paper | N/A |
| pMDC43-YFC-AtHSP90.3 | This paper | N/A |
| pMDC43-YFC-BBX24 | This paper | N/A |
| pMDC43-YFN-JAZ3 | This paper | N/A |
| pEarleyGate104 | Earley et al.[53] | N/A |
| pEarleyGate203 | Earley et al. [53] | N/A |
| pEarleyGate104-AtRPAP3 | This paper | N/A |
| pEarleyGate104-AtRPAP3mut2 | This paper | N/A |
| pEarleyGate104-AtRPAP3mut6 | This paper | N/A |
| pEarleyGate104-AtRuvBL2a | This paper | N/A |
| pEarleyGate104-AtHSP90.3 | This paper | N/A |
| pEarleyGate203-AtRuvBL2a | This paper | N/A |
| pEarleyGate203-AtHSP90.3 | This paper | N/A |
| pMDC123-pAtHSP90.3:6xHis-TEV-3xFLAG-AtHSP90.3 | This paper | N/A |
| pGADT7-AtRPAP3 | This paper | N/A |
| pGADT7-AtRuvBL1 | This paper | N/A |

| | | |
|---|---|---|
| pGADT7-AtRuvBL2a | This paper | N/A |
| pGADT7-AtHSP90.3 | This paper | N/A |
| pGADT7-AtURI | This paper | N/A |
| pGADT7-UXT | Gómez-Mínguez et al.[31] | N/A |
| pGADT7-PDRG1 | Gómez-Mínguez et al.[31] | N/A |
| pGADT7-PFD2 | Gómez-Mínguez et al.[31] | N/A |
| pGADT7-PFD6 | Gómez-Mínguez et al.[31] | N/A |
| pGADT7-ASDURF | This paper | N/A |
| pGBKT7-AtRPAP3 | This paper | N/A |
| pGBKT7-AtRuvBL2a | This paper | N/A |
| pGBKT7-AtHSP90.3 | This paper | N/A |
| pGBKT7-AtURI | Gómez-Mínguez et al.[31] | N/A |
| pGBKT7-UXT | This paper | N/A |
| pGBKT7-PDRG1 | This paper | N/A |
| pGBKT7-PFD2 | This paper | N/A |
| pGBKT7-PFD6 | This paper | N/A |
| pGBKT7-AtRPAP3mut2 | This paper | N/A |
| pGBKT7-AtRPAP3mut6 | This paper | N/A |
| pET-15b | Novagen | Cat#-69661 |
| pCDFDuet-1 | Novagen | Cat#-71340 |
| pRSFDuet-1 | Novagen | Cat#-71341 |
| pET-15b-AtRuvBL1 | This paper | N/A |
| pCDFDuet-1-AtRuvBL2 | This paper | N/A |
| pRSFDuet-1-AtRPAP3 | This paper | N/A |
| Software and algorithms | | |
| Benchling | Benchling | https://www.benchling.com/ |
| Zeiss ZEN Software | Zeiss | https://www.zeiss.com/microscopy/int/products/microscope-software/zen-lite.html |
| ImageJ | ImageJ | https://imagej.nih.gov/ |
| Modeller (version 9.23) | Modeller | https://salilab.org/modeller/9.23/release.html |
| PyMOL 2.4 | Pymol | https://www.pymol.org/ |
| Biodock | Biodock | https://www.biodock.ai/ |

| | | |
|---|---|---|
| PRISM 10 | GraphPad | https://www.graphpad.com/ |
| RELION | Zivanov et al.[54] | https://relion.readthedocs.io/en/release-5.0/ |
| cryoSPARC | Punjani et al.[55] | https://cryosparc.com/ |
| USCF Chimera | Pettersen et al.[56] | http://www.rbvi.ucsf.edu/chimera/ |
| ISOLDE | Croll[57] | https://tristanic.github.io/isolde/ |
| Coot | Emsley et al.[58] | https://www2.mrc-lmb.cam.ac.uk/personal/pemsley/coot/ |

## EXPERIMENTAL MODEL AND STUDY PARTICIPANT DETAILS

### Bacterial experimental models

The widely distributed strain of *Escherichia coli* TOP10 was used for gene cloning. *E. coli* LOBSTR-BL21(DE3)-RIL strain was used for recombinant protein expression. Both strains were grown in standard LB media at 37ºC (TOP10) or a lower temperature depending on the protein being expressed (LOBSTR-BL21(DE3)-RIL).

The strain *Agrobacterium tumefaciens* GV3101 (pM90 C58) was used for *Arabidopsis* transformation and for transient expression in *N. benthamiana* leaves. This strain was grown at 28ºC in standard LB media supplemented with gentamycin and rifampicin to select for the strain and the antibiotic that selects for the expression plasmid.

### Yeast experimental models

*Saccharomyces cerevisiae* strains Y2HGold and Y187 were used for Y2H assays. Yeast cells were grown at 28ºC in either complete YPD medium or in Synthetic Defined (SD) medium supplemented with Leu, Trp and His. Both YPD and SD media were supplemented with 2% (v/v) Glc.

### Plant experimental models

*Arabidopsis* mutants and transgenic lines are in Col-0 background. The *AtRPAP3* mutant allele *tpr5-2* and the transgenic line *pAtRPAP3:AtRPAP3-GFP tpr5-2* have been described

[38]. *Arabidopsis* seeds were surface sterilized with a solution of 70% (v/v) ethanol / 0.05% (v/v) Triton-X 100 followed by 100% (v/v) ethanol for 5 min each in a rotating wheel at RT. Seeds were dried in a flow cabinet under sterile conditions and sown in MS plates supplemented with 1% sucrose. Seeds were stratified at 4ºC for 2-4 days in the dark. Germination was induced by placing the plates in a growth cabinet (Panasonic MLR-352 PE) at 22ºC and continuous white, fluorescent light (50 μmol $m^{-2}$ $s^{-1}$). The seedlings were grown under these conditions for the duration of the experiment.

*Nicotiana benthamiana* wild-type seeds were sown in pots filled with regular soil mixture from a local provider and covered for a week with a plastic humidity dome after watering. Plants were grown in a growth room under 16 hours of white, fluorescent light (120 μmol $m^{-2}s^{-1}$) and 8 hours of darkness at 24ºC (light) and 20ºC (darkness).

**METHOD DETAILS**

**Preparation of transgenic *Arabidopsis* lines**

We prepared an *Arabidopsis* line expressing *pAtHSP90.3:6xHis-TEV-3xFLAG-AtHSP90.3* in the *pAtRPAP3:AtRPAP3-GFP tpr5-2* background. To make the *pAtHSP90.3:6xHis-TEV-3xFLAG-AtHSP90.3* construct, we amplified by PCR a genomic fragment starting -1141 bp upstream of the *AtHSP90.3* transcription start site until the stop codon, which was included, and was cloned by Gateway first into the pDONR207 and then into the destination vector pMDC123 [59]. Next, a NcoI site was introduced at the starting ATG by PCR, which was used to insert a DNA fragment containing the *6xHis-TEV-3xFLAG* sequence by In-Fusion technology (Takara). This DNA fragment encodes the TEV protease recognition site between the 6xHis and 3xFLAG sequences. We inserted the 6xHis-TEV-3xFLAG tag at the N-terminus of the chaperone because the C-terminal tag may interfere with interaction with partners, especially those that interact with the C-terminal end, such as RPAP3, as has been observed in humans [45]. The construct was introduced into *pAtRPAP3:AtRPAP3-GFP tpr5-2* plants via *Agrobacterium tumefaciens* C58 transformation. Transgenic plants were selected in 1/2 Murashige and Skoog (MS) medium containing basta herbicide. All oligonucleotides used for cloning are shown in Table S3.

**Identification of PFD6 and AtRPAP3 interactors**

The CDS with stop codon of AtRPAP3 was amplified by PCR from a cDNA pool of one-week-old *Arabidopsis* seedlings, cloned into pDONR207 and transferred into the pKNGS_rhino vector [33] by Gateway to create a $GS^{rhino}$-AtRPAP3 fusion. The $GS^{rhino}$-PFD6 construct was prepared using pENTR223-PFD6 [60]. As control construct, pKGNS_rhino fused to a nonsense stuffer sequence was used to express $GS^{rhino}$ alone [31]. *Agrobacterium tumefaciens* C58 cells carrying pKNGS_rhino-PFD6, pKNGS_rhino-AtRPAP3 and the control construct were used to transform PSB-D cell suspensions [33]. 11 g of cells expressing pKNGS_rhino-PFD6 from each of two biological replicates were used for tandem affinity purification [33]. The purified proteins were loaded into a 12% PAGE and the hand-cut bands were subjected to in-gel trypsin digestion with Proteineer DP (Bruker). The digested peptides were separated based on their hydrophobicity using a NanoLC-Ultra HPLC coupled to a 5600 TRIPLE TOF mass spectrometer (Thermo Fisher Scientific). A reversed-phase LC Acclaim PepMap 100 C18 LC trap column (Thermo Fisher Scientific) and an ACQUITY UPLC M-Class Peptide CSH C18 column (Waters) were used for liquid chromatography. The protein search was performed with the MASCOT search engine. Peptide sequences identified with an FDR ≤ 1% at the peptide level were considered as significant. Peptide digestion, separation and protein identification were performed by the Proteomics Facility of the Centro Nacional de Biotecnología (Madrid, Spain). For TAP experiments with *Arabidopsis* PSB-D cell suspensions and fusions with the $GS^{rhino}$ tag, it is common to rely on a background list based on the occurrence of proteins in 543 TAP experiments with 115 different bait proteins [33]. These were categorized into 62 bait groups based on their functional relationship and a protein was considered as non-specific if it occurred in three or more bait groups [33]. The criterion we have followed in this work to consider a protein as a specific interactor was that it was identified in the two biological replicates and was not present in three or more bait groups.

Single affinity purifications (AP) with 7 g of cells expressing pKNGS_rhino-AtRPAP3 and the control construct from each of the three biological replicates were performed according to the previously described protocol [31,61]. The purified proteins were loaded into a 10% PAGE and the hand-cut bands were subjected to in-gel trypsin digestion. The digested peptides were separated by liquid chromatography using Ultimate 3000 Dionex UHPLC (Thermo Fisher Scientific) coupled to an Orbitrap Fusion mass spectrometer

(Thermo Fisher Scientific). A C18 PepMap100 precolumn (Thermo Fisher Scientific) and a C18 Acclaim PepMap RSLC column (Thermo Fisher Scientific) were used for liquid chromatography. Protein searches were performed using the SEQUEST HT search engine with a mass tolerance of 10 ppm. A decoy search with an FDR ≤ 1% was used for peptide identification. Peptide digestion, separation and protein identification were performed by the Servicio de Proteómica of the Universidad de Córdoba (Spain). The AP-MS analysis of $GS^{rhino}$-AtRPAP3 was performed together with that of $GS^{rhino}$-AtURI and $GS^{rhino}$-UXT, therefore the $GS^{rhino}$ control is the same as reported [31] (Table S1). We considered proteins as interactors if they met the following criteria. They were present in at least two out of three replicates with at least four unique peptides in one of them, the replicate with the maximum number of peptides was four times higher than the maximum number found in the $GS^{rhino}$ control, and the replicate with the minimum number of peptides was twice the number found in the replicate with fewer peptides in the $GS^{rhino}$ control.

**Yeast two-hybrid assays**

The CDSs with stop codon of AtRuvBL1, AtRuvBL2a, AtHSP90-3 and ASDURF were amplified by PCR from a cDNA pool of one-week-old wild-type Col-0 *Arabidopsis* seedlings and cloned by Gateway into pDONR207. The AtRPAP3mut2 version, in which the codons encoding R428 and M431 were changed to encode A, was produced by overlapping PCR and cloned into pDONR207. The CDS of the AtRPAP3mut6 version, in which the codons encoding N92, N122, K129, K152, R156 and E181 were changed to encode A, was synthesized by Integrated DNA Technologies (Belgium) and cloned into pDONR207. The CDSs of AtRPAP3, AtRuvBL1, AtRuvBL2a, AtHSP90-3 and ASDURF were transferred to the pGADT7-GW and pGBKT7-GW destination vectors using Gateway LR Clonase II enzyme mix to produce fusion proteins of the Gal4-activation domain (AD) and GAL4 DNA-binding domain (BD), respectively. The CDS of AtURI, UXT, PFD2 and PFD6 cloned into pGADT7-GW and pGBKT7-GW have been previously described [31]. The CDSs of AtRPAP3mut2 and AtRPAP3mut6 were transferred to the pGBKT7-GW destination vector using Gateway LR Clonase II enzyme mix. The expression vectors derived from pGADT7 and pGBK7 were introduced into Y187 and Y2HGold yeast strains, respectively. The transformants were selected with Synthetic Defined (SD) medium,

which lacked leucine (-Leu) or tryptophan (-Trp). Haploid yeast cells were mated to obtain diploid cells by selection in SD-Leu-Trp medium. Protein interactions were tested by the nutrient requirement of histidine (His) in SD-Leu-Trp-His plates.

**Confocal microscopy**

The CDSs of AtRPAP3, AtRuvBL2a and AtHSP90.3 were transferred by Gateway into the pEarleyGate-104 vector [53] to fuse YFP to the N-terminal end of each protein. The AtRPAP3 CDS was also transferred into the vector pH7WGR2 (gatewayvectors.vib.be/collection/ph7wgr2) to fuse mRFP to its N-terminus. Leaves of three-week-old *Nicotiana benthamiana* plants grown under a 16 hours light: 8 hours dark photoperiod were infiltrated with *Agrobacterium tumefaciens* C58 carrying constructs to express AtRPAP3, AtRuvBL2a or AtHSP90-3 fused to YFP or RFP, and the p19 silencing suppressor. Leaf confocal fluorescence was recorded on the third day after agroinfiltration using a Zeiss Axio-Observer 780 Pascal confocal microscope. The YFP signal was excited with an argon laser at the wavelength of 488 nm, and its emission was detected at 505-530 nm. The RFP signal was excited with an argon laser at the wavelength of 555 nm, and its emission was detected at 575-600 nm. Chloroplasts autofluorescence was detected between 675 and 760 nm.

**Bimolecular fluorescence complementation assay**

The CDS of AtRPAP3 and that of AtRuvBL2a and AtHSP90.3 were transferred into pMDC43-YFN and pMDC43-YFC vectors, respectively [62], by Gateway for bimolecular fluorescence complementation (BiFC) assays. *Agrobacterium tumefaciens* C58 cultures containing combinations of these plasmids and those of negative controls (at a ratio of 1:1 up to a total optical density of 0.1) were used to infiltrate 3-week-old *N. benthamiana* leaves. Three days after infiltration, confocal images were collected using Zeiss Axio-Observer 780 Pascal confocal microscope. Reconstituted YFP signal was detected in abaxial epidermal cells at 503-517 nm after excitation with an Argon laser (488 nm).

**Cloning, expression and purification of recombinant proteins**

The CDS of AtRuvBL1 was cloned into a modified pET-15b vector (Novagen) including a N-terminal histidine tag followed by tobacco etch virus (TEV) protease site, and untagged AtRuvBL2a was cloned into pCDFDuet-1 vector (Novagen) using standard cloning protocols. Deletion mutants AtRuvBL1-ΔDII and AtRuvBL2a-ΔDII, lacking residues 130-236 and 129-234 respectively, were generated from the AtRuvBL1 and AtRuvBL2a constructs by site-directed mutagenesis, replacing the deleted regions by a Gly-Pro-Pro-Gly linker. AtRPAP3 was cloned into pRSFDuet-1 vector (Novagen) with a N-terminal His-tag followed by an IF2D1 tag (translation initiation factor 2 domain 1) and a TEV protease site, and a C-terminal Strep-tag with human rhinovirus 3C (HRV 3C) protease site using the IVA cloning methodology [63].

Expression of the AtRuvBL1-AtRuvBL2a complex was carried out by co-expression of the two plasmids containing the individual proteins in *E. coli* LOBSTR-BL21(DE3)-RIL cells and induction with 0.1 mM isopropyl-β-D-1-thiogalactopyranoside (IPTG) for 4 hours at 28ºC. Cells were collected by centrifugation at 5,000 rpm and 4ºC, and lysed in 50 mM Tris-HCl, 300 mM NaCl, 10% (v/v) glycerol, 0.1% (v/v) NP-40 buffer supplemented with lysozyme (0.3 mg/ml), benzonase (250 U/µl) (Novagen) and cOmplete® EDTA-free protease Inhibitor Cocktail (Roche) by sonication. After clarification at 50,000 rpm during 1 hour at 4ºC, lysate was filtered through a 0.45 µm device and loaded onto a HisTrap HP (Cytiva) column equilibrated in 40 mM Tris-HCl, 200 mM NaCl, 5% (v/v) glycerol, 20 mM imidazole buffer. Elution was performed using a 20-500 mM imidazole gradient, and fractions containing the AtRuvBL1-AtRuvBL2a complex were pooled and dialyzed in 50 mM Tris-HCl pH 7.4, 150 mM NaCl, 10% (v/v) glycerol buffer over night at 4ºC. The sample was further purified using a Superose 6 Increase GL 3.2/100 column (Cytiva) equilibrated in 50 mM Tris-HCl pH 7.4, 150 mM NaCl buffer.

AtRuvBL1-ΔDII – AtRuvBL2a-ΔDII truncated complex, that lacks the OB-fold domains with the DII domains of both proteins were produced and purified by co-expressing AtRuvBL1-ΔDII and AtRuvBL2a-ΔDII using the same protocol described for the wild-type complex.

AtRPAP3 was produced by expression in *E. coli* BL21 (DE3) strain by induction with 0.25 mM IPTG at 16ºC for 18 hours. Cells were harvested and lysed by sonication in 50 mM HEPES, 500 mM NaCl, 10% (v/v) glycerol, 0.5% (v/v) NP-40, 1 mM DTT buffer supplemented with lysozyme (0.3 mg/ml), benzonase (250 U/µl) (Novagen) and

cOmplete® EDTA-free protease Inhibitor Cocktail (Roche). Cleared lysate was loaded into a HisTrap HP (Cytiva) column equilibrated in 25 mM HEPES pH 8, 300 mM NaCl, 20 mM imidazole, and purified protein was eluted with a 20-500 mM imidazole gradient. Pooled fractions containing AtRPAP3 were loaded onto a StrepTactin®XT 4Flow® high-capacity column (IBA Lifesciences) equilibrated in 25 mM HEPES pH 8, 300 mM NaCl, 1 mM DTT buffer and eluted with the same buffer supplemented with 50 mM biotin. Purified AtRPAP3 was concentrated with an Amicon® Ultra-4 30,000 MWCO centrifugal filter unit (Millipore) and size exclusion purified in a Superose 6 Increase 10/300 GL (Cytiva) column equilibrated in 25 mM HEPES pH 8, 300 mM NaCl, 1 mM DTT.

The AtRuvBL1-AtRuvBL2a-AtRPAP3 (R2T) complex was produced by co-expression of AtRuvBL1, AtRuvBL2a and AtRPAP3 in *E. coli* BL21 (DE3) cells and induction with 0.25 mM IPTG at 17ºC for 18 hours. The complex was purified by pulling down from the Strep-tag in AtRPAP3 with a StrepTactin®XT 4Flow® column (IBA Lifesciences) using the same protocol described for AtRPAP3. Fractions containing the R2T complex were dialyzed in 25 mM HEPES pH 8, 300 mM NaCl, 1 mM DTT, 10% (v/v) glycerol buffer, and further purified in a Superose 6 Increase 10/300 GL (Cytiva) column equilibrated in 25 mM HEPES pH 8, 300 mM NaCl, 1 mM DTT.

The identity of the purified bands of all recombinant proteins was verified by mass spectrometry.

**ATPase assays**

Activity of the purified AtRuvBL1-AtRuvBL2a complex was tested by measuring the ATP hydrolysis in a continuous spectrophotometric pyruvate kinase-lactate dehydrogenase-coupled assay, based on the regeneration of the hydrolyzed ATP coupled to oxidation of NADH. NADH absorbance at 340 nm was measured using a CLARIOstar Plus plate reader (BMG Labtech) in time course experiments, and ATP hydrolysis rates were calculated from the slope of the decreasing curves. Assays were performed at 37ºC in 100 µl reactions in buffer 50 mM Tris-HCl pH 7.4, 150 mM NaCl, 20 mM $MgCl_2$, containing 2 mM phosphoenolpyruvate (PEP), 0.5 mM NADH, 0.04 U/µl pyruvate kinase/0.05 U/µl lactic dehydrogenase (Sigma-Aldrich) and 5 mM ATP. Hydrolysis reactions were started by addition of 3 µM of AtRuvBL1-AtRuvBL2a (concentration calculated considering monomers), 1 µM AtRPAP3 (control experiment) or 3 µM of AtRuvBL1-AtRuvBL2a plus

1 µM AtRPAP3, and carried out for 50 min. A similar protocol was followed for testing the effect of the CB-6644 small compound in the ATPase activity of AtRuvBL1-AtRuvBL2a, in reactions containing 3 µM of the complex and increasing concentrations of the inhibitor (0, 0.01, 0.1, 1.0, 10 and 100 µM). ATP turnover (mol ATP/mol protein) indicated in $min^{-1}$ was calculated for a time interval during which the absorbance decrease was linear. Values in the graph are indicated as percentage of the rate of the wild-type protein.

**Negative staining EM**

The AtRuvBL1-ΔDII-AtRuvBL2a-ΔDII truncated complex was analyzed by EM of negative stained samples after size exclusion fractionation in a Superose 6 Increase 3.2/300 column equilibrated in 20 mM Tris-HCl pH 8, 200 mM NaCl, 1 mM DTT buffer. 3 µl of several fractions from the chromatography (0.01 mg/ml) were deposited onto freshly glow-discharged carbon-coated 400 mesh copper EM grids (Electron Microscopy Sciences) and stained using 2% (w/v) uranyl formate. Grids were imaged on a Tecnai 12 transmission electron microscope (Thermo Fisher Scientific) equipped with a lanthanum hexaboride cathode and operated at 120 keV. For the samples incubated with ATP and the CB-6644 inhibitor, the R2T complex (final concentration 0.025 mg/ml) was incubated with a 15-fold molar excess of CB-6644, 20 mM ATP and 20 mM $MgCl_2$. Control samples of R2T apo (without addition of nucleotide), and samples of R2T incubated only with 20 mM ATP and 20 mM $MgCl_2$ were also analysed. Negative stained grids for the three samples were prepared and imaged as described.

**Cryo-EM**

3 µl of freshly purified protein complex, either AtRuvBL1-AtRuvBL2a or R2T, at 0.8 mg/ml were applied to glow discharged Quantifoil® 300 mesh R 0.6/1 grids and flash frozen in liquid ethane using FEI Vitrobot MAG IV (Thermo Fisher Scientific). For AtRuvBL1-AtRuvBL2a complex, 1001 movies were collected on a JEOL JEM-2200FS microscope operating at 200 kV, equipped with a K3 counting camera (Gatan). Calibration and automatic data collection were performed with SerialEM (University of Colorado) at a nominal magnification of ×40k, physical pixel size of 0.9772 Å, a total dose of 40 $e^-/Å^2$,

and 40 fractions. Autofocus was performed using an objective defocus range between −1.5 and −3.0 µm (Table S2).

For the R2T complex, 6139 movies were collected in a Titan Krios equipped with a Falcon 4i detector (Thermo Fisher Scientific) and Selectris X energy filter at eBIC (Diamond Light Source, Oxford, UK) in counting mode, and a slit width of 5 eV. Microscope calibrations and automatic data acquisition were performed with EPU software (Thermo Fisher Scientific) at a nominal magnification of ×130k, physical pixel size of 0.921 Å, a total dose of 50.12 $e^{-}/Å^2$, 8.05 $e^{-}/Å^2/s$ and 50 fractions. Autofocus was performed using an objective defocus range between −1.5 and −3.0 µm. Cryo-EM images were collected at the Diamond Light Source cryo-EM facility at the UK's National Electron Bio-imaging Center (eBIC).

**Image processing**

Local drift was corrected on images of the AtRuvBL1-AtRuvBL2a complex using MotionCor2 (5 × 5 patches) and dose-weighting of fraction stacks [64]. Contrast transfer function (CTF) parameters of drift-corrected images were determined with Gctf [65]. The 179,410 best quality particles were selected after 2D classification in RELION of the initial data set containing 297,450 particles (Figure S5C). Initial model was obtained using cryoSPARC [55], and 3D-refined with RELION. After 3D classification, the best particles were selected and further refined. Focused 3D refinement on the top and bottom rings of the dodecameric volume was performed to obtain 4.7 Å and 6.7 Å maps, respectively, using gold-standard methods and the Fourier Shell Correlation (FSC) cut-off of 0.143.

Images of the R2T complex were local drift corrected and CTF parameters were determined as described. A subset of manually picked particles was used to generate reference-free 2D averages in RELION [54] that were further used for template-based automatic particle picking. R2T complex initial data set containing 2,334,954 particles was 2D-classified in RELION, and the 788,672 best quality particles were selected (Figure S8 and Table S2). *Ab initio* 3D model was generated from the selected particles using cryoSPARC [55], and used as reference for a consensus 3D-refinement in RELION. A subset of 481,879 particles was selected after getting rid of junk particles by 3D-classification of the dodecameric R2T model and further 3D-refined. Densities corresponding to the RBD domain of AtRPAP3 bound to the AtRuvBL1-AtRuvBL2a dodecamer were poorly

defined, so a focused 3D-classification protocol was applied using a mask containing the hexameric top ring and three RBD densities, defining a population of particles with no AtRPAP3 bound (296,837 particles, 61.6 %) and 3 populations containing one RBD molecule bound each in different positions (185,042 particles, 38.4 %) (Figure S8). The RBD-containing particles were aligned to the same position based on the RBD density and focused 3D-refined. After applying the same focused 3D-classification protocol to the bottom hexamer of the complex, two dodecameric populations were identified, one containing a second RBD density in the bottom hexamer (complex 1, 7.75 Å; 18%) and one with no density for RBD in bottom ring (complex 2, 8.18 Å; 82%). Particles with the top ring RBD density aligned were 3D-refined with a mask engaging the top ring R2T, and after iterative rounds of CTF refinement and Bayesian Polishing in RELION, a cryo-EM map for the top ring R2T complex was obtained at an average resolution of 3.73 Å map using gold-standard methods and the Fourier Shell Correlation (FSC) cut-off of 0.143 (Figure S9A).

For the negative stained images of the AtRuvBL1-ΔDII-AtRuvBL2a-ΔDII truncated complex, 316 micrographs were recorded at 61,320 x nominal magnification and 2.5 Å/pix on a 4k × 4 k TemCam-F416 CMOS camera (TVIPS), and 90,328 particles were automatically selected and subjected to 2D classification using cryoSPARC [55]. For the R2T apo sample used as a control, 232 micrographs of the negative stained sample were collected from which 24,067 particles were selected; 412 micrographs and 115,515 particles for the R2T-ATP sample; and 136 micrographs and 84,490 particles for R2T-ATP-CB-6644 sample. Particles were subjected to 2D classification using cryoSPARC [55], and particles containing in either dodecameric or hexameric side views of the complex were counted based on the number of particles assigned to each 2D class.

**Model building**

The high-resolution cryo-EM map of the top ring of the R2T complex was used for model building using as starting models the atomic models of the AtRuvBL1 (AF-Q9FMR9-F1), AtRuvBL2a (AF-Q9FJW0-F1) and AtRPAP3 (AF-Q5XF05-FA) proteins generated in AlphaFold2 [66]. Using the model of the human R2TP complex as template (PDB 6FO1), 3 copies of the AtRuvBL1 model, 3 copies of AtRuvBL2a and one AtAtRPAP3 RBD domain were aligned to create the hexameric complex and rigid fitted in the cryo-EM map of

R2T using USCF Chimera [56]. An initial step of automatic refinement was done in phenix.real_space_refinement [67], followed by interactive model building using ISOLDE [57] and manual refinement of the seven chains in Coot [58]. A final step of automatic refinement was done in phenix.real_space_refinement to improve the geometries of the model (Table S2).

Using the TPR2 domain of human RPAP3 as a template (PDB code: 6FDP), the structure of the TPR domain of AtRPAP3 was generated using Modeler (version 9.23) [68]. The predicted structure of the TPR domain of AtRPAP3 was aligned with the human model (PDB code: 6FDP) and polar contacts between the TPR domain of AtRPAP3 and the MEEVD peptide were identified using PyMOL 2.4 software (pymol.org).

**Protein co-immunoprecipitation assays**

The CDSs of AtRuvBL2a and AtHSP90.3 were transferred into the pEarleyGate-203 vector to create Myc fusions [53]. The CDSs of AtRPAP3mut2 and AtRPAP3mut6 were transferred into pEarleyGate-104 to produce the YFP-AtRPAP3mut2 and YFP-AtRPAP3mut6 fusions by Gateway.

Leaves of three-week-old *N. benthamiana* plants were infiltrated with different mixtures of *Agrobacterium tumefaciens* C58 cultures carrying the expression vectors and the p19 silencing suppressor. Three days after infiltration, the leaves were collected and frozen in liquid nitrogen. 1 ml of the frozen tissue was homogenized in 0.5 ml of extraction buffer containing 50 mM Tris-HCl pH 7.5, 150 mM NaCl, 0.25% (v/v) Triton X-100, 2 mM PMSF and 1X cOmplete® EDTA-free protease inhibitor cocktail (Roche). The extracts were placed on ice for 15 minutes and then centrifuged 2 times at maximum speed in a benchtop centrifuge at 4ºC. 150 µg of total proteins were denatured in 1 volume of 2X Laemmli buffer and kept for later use as input samples. In addition, 1 mg of total protein was incubated with 25 µl of GFP-Trap® Magnetic Beads (ChromoTek) in 1 ml of extraction buffer at 4 ºC for 2 hours in a rotating wheel. The beads were separated with a magnet and the supernatant was discarded. The beads were resuspended in 1 ml wash buffer (Tris-HCl pH 7.5, 350 mM NaCl, 0.25% Triton X-100 [v/v]) and incubated at 4ºC for 5 min in a rotating wheel. This washing step was repeated four times. The proteins were then eluted by incubating the beads with 70 µl 2X Laemmli for 5 min at 95 ºC. For analysis, 63 µl of the immunoprecipitated samples (representing

90% of the total) were loaded onto a 10% SDS-PAGE together with 50 µg of the input sample. After electrophoresis, the proteins were transferred to a PVDF membrane and immunodetected with an anti-Myc-HRP antibody (Myc-HRP, 1:5000, Thermo Fisher Scientific). The remaining 10% of the immunoprecipitated samples together with 50 µg of the input were subjected to the same procedure but probed with an anti-GFP antibody (JL-8, 1:5000, Clontech). After incubation with SuperSignal™ West Femto (Thermo Fisher Scientific), chemiluminescence was visualized with the ImageQuant 800 (Amersham).

To test the interaction between AtRPAP3 and AtHSP90.3 in the presence or absence of GDA, *Arabidopsis* lines expressing AtRPAP3-GFP/6xHis-TEV-3xFLAG-AtHSP90.3 and AtRPAP3-GFP (control) were used. 7-day-old *Arabidopsis* seedlings grown in 1/2 MS plates under continuous light (50–60 µmol $m^{-2}$ $s^{-1}$) at 22°C were transferred to liquid 1/2 MS medium containing 20 µM GDA or mock solution (DMSO) for 24 hours in darkness. Total proteins were immunoprecipitated with anti-FLAG antibody-coated magnetic beads (Sigma). The proteins were detected with anti-GFP and anti-FLAG antibodies (Sigma). The procedure was performed as described above.

**Growth assay in response to geldanamycin**

Seeds of WT and *tpr5-2* were germinated for 2 days under continuous light (50–60 µmol $m^{-2}$ $s^{-1}$) at 22°C. After two days, seedlings were transferred to plates containing 1/2 MS medium supplemented with a mock solution (DMSO) or 10 µM GDA (MedChem, HY-15230) and maintained under the same conditions. Photos were taken 10 days after treatment. Biodock for AI image analysis (biodock.ai) was used to quantify the area of each plant for each genotype and condition. An unpaired t-test was performed and area values were plotted using Graphpad Prism 8.0.2.

**QUANTIFICATION AND STATISTICAL ANALYSIS**

All statistical analyses were performed using GraphPad Prism 8.0.2 software. In Figure 3B, the values represent the mean ± SD of three replicates. One-way ANOVA test was used for the comparison of statistical significance. In Figure 5B, the values represent mean ± SD of three replicates. Statistical significance comparison was estimated with One-way ANOVA test. In Figure 8B, the values represent the mean. The statistical P-

values in Figure 8B were determined using an unpaired t-test. Cryo-EM data collection and refinement statistics are summarized in Table S2.

A

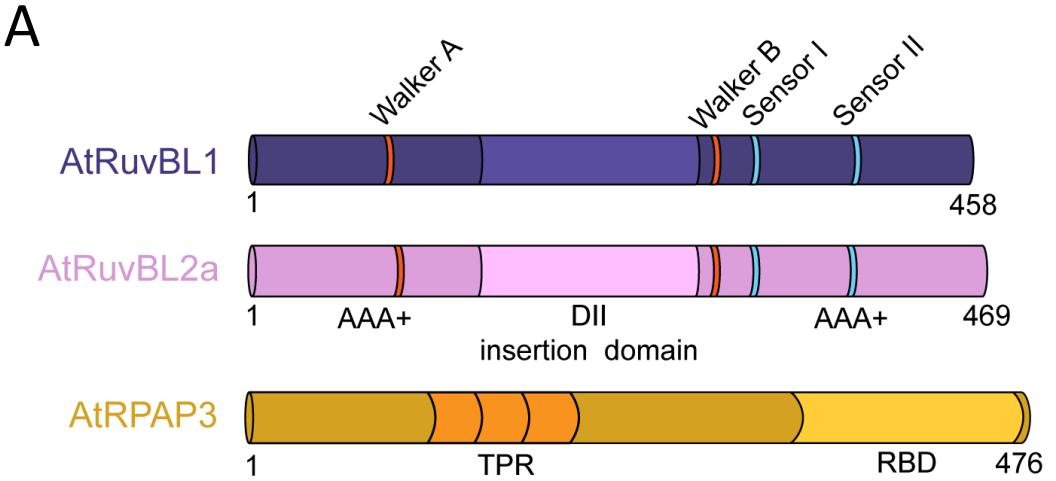
Walker A
Walker B
Sensor I
Sensor II
AtRuvBL1
1
458
AtRuvBL2a
1
AAA+
DII
insertion domain
AAA+
469
AtRPAP3
1
TPR
RBD
476

B

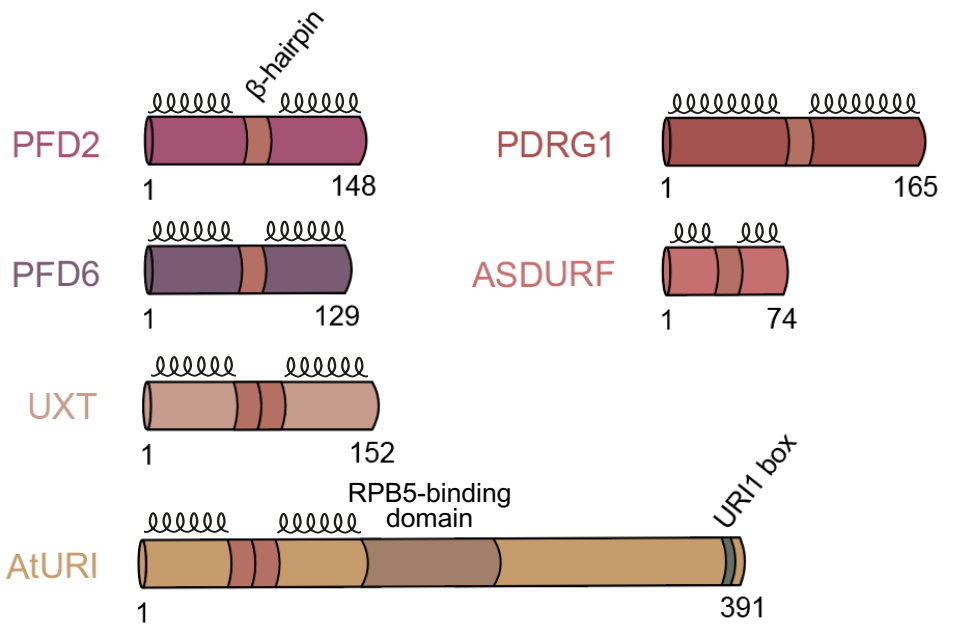
β-hairpin
PFD2
1
148
PDRG1
1
165
PFD6
1
129
ASDURF
1
74
UXT
1
152
RPB5-binding domain
URI1 box
AtURI
1
391

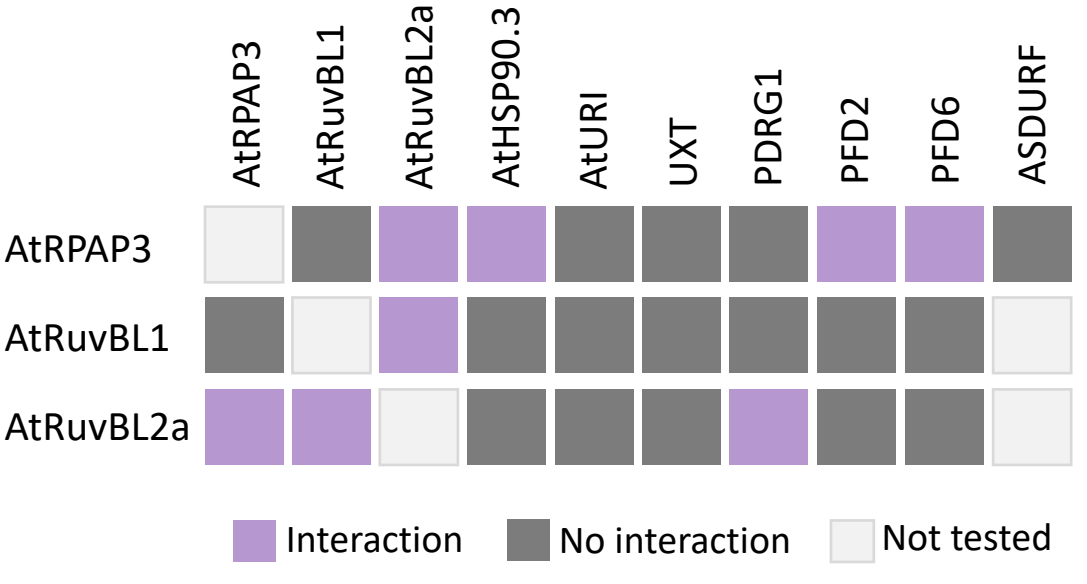
AtRPAP3
AtRuvBL1
AtRuvBL2a
AtHSP90.3
AtURI
UXT
PDRG1
PFD2
PFD6
ASDURF
AtRPAP3
AtRuvBL1
AtRuvBL2a
Interaction
No interaction
Not tested

A

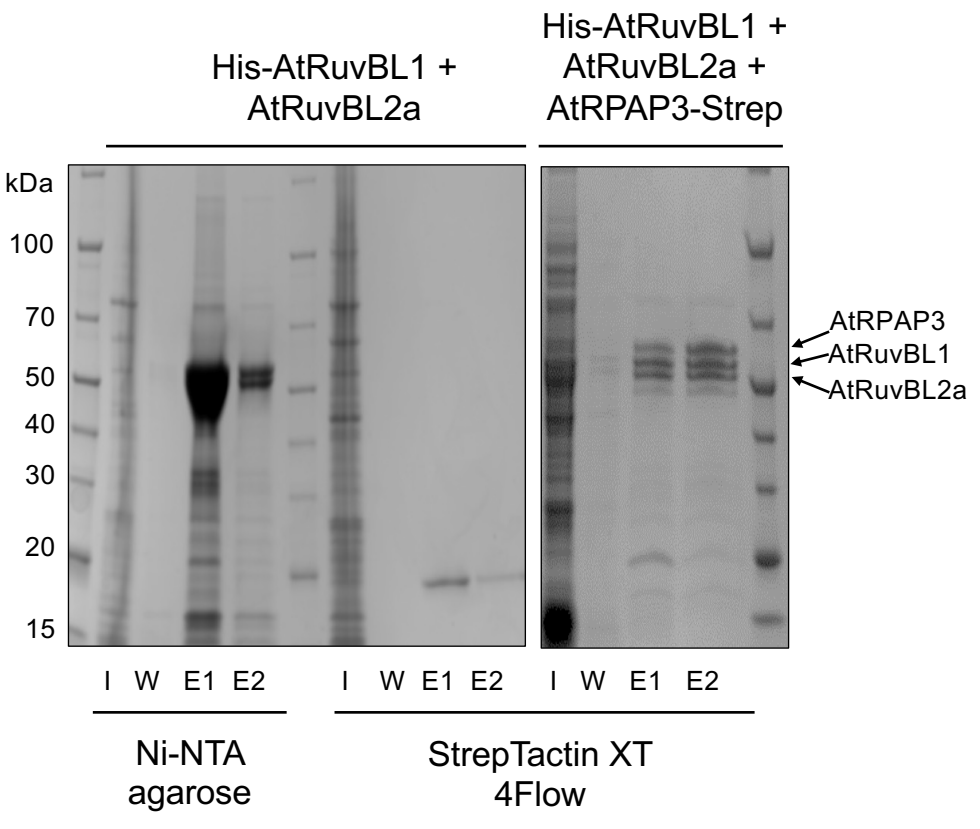
His-AtRuvBL1 +
AtRuvBL2a
His-AtRuvBL1 +
AtRuvBL2a +
AtRPAP3-Strep
kDa
100
70
50
40
30
20
15
AtRPAP3
AtRuvBL1
AtRuvBL2a
I W E1 E2
I W E1 E2
I W E1 E2
Ni-NTA
agarose
StrepTactin XT
4Flow

B

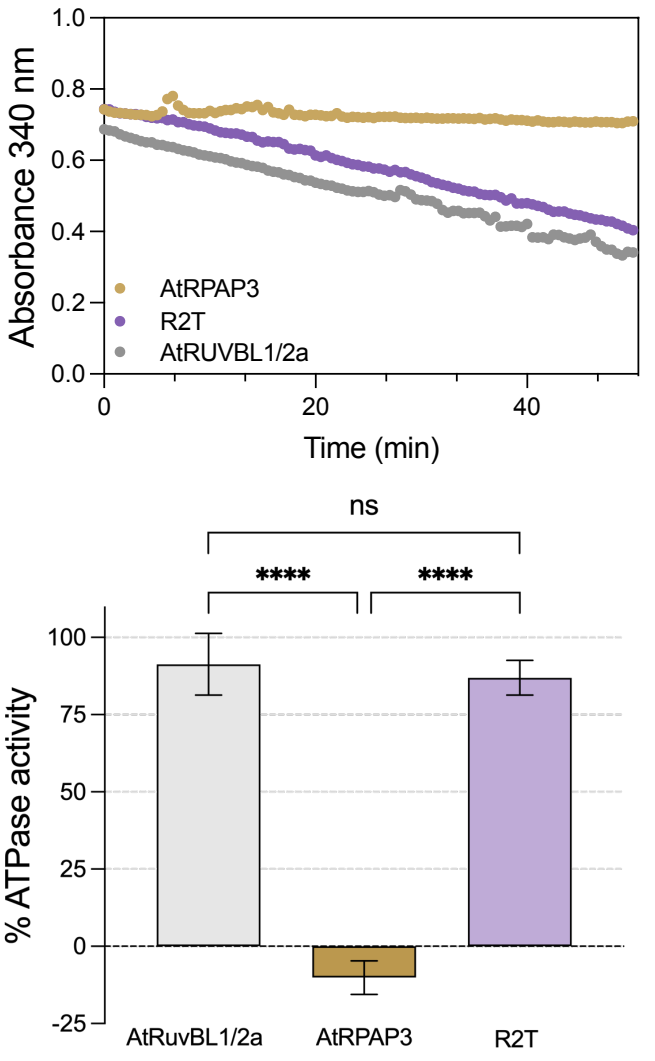
Absorbance 340 nm
1.0
0.8
0.6
0.4
0.2
0.0
0
20
40
Time (min)
AtRPAP3
R2T
AtRUVBL1/2a
ns
****
****
% ATPase activity
100
75
50
25
0
-25
AtRuvBL1/2a
AtRPAP3
R2T

A

YFP-AtRPAP3

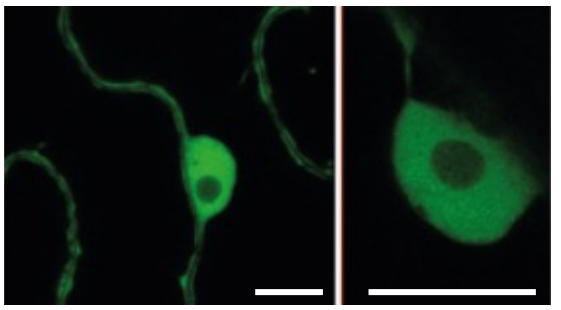

B

YFP-RuvBL2a

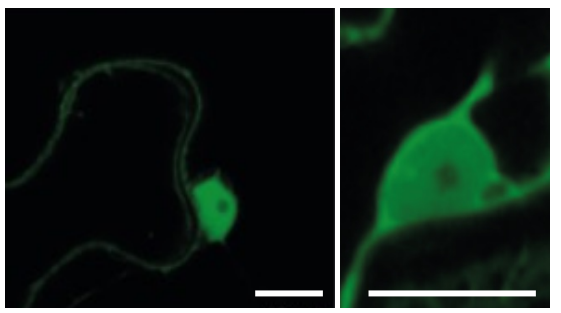

D

YFP-AtHSP90.3

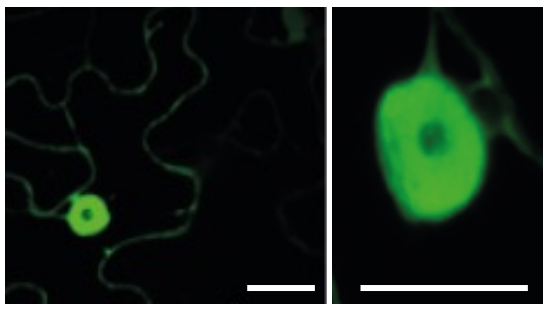

C

YFC-AtRuvBL2a / YFN-AtRPAP3

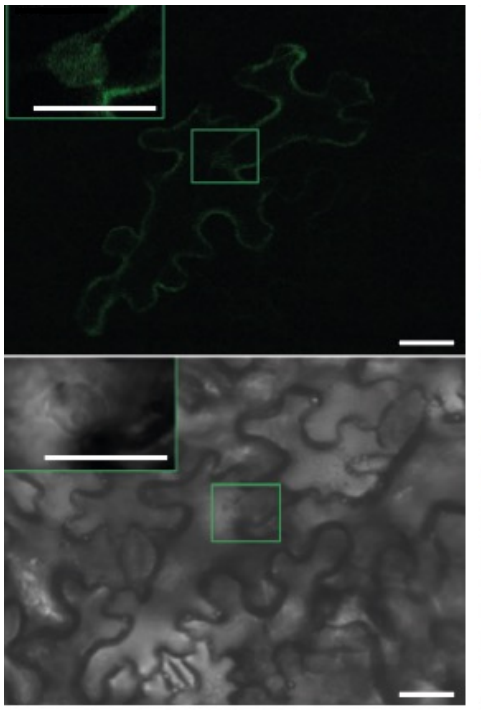

E

YFC-AtHSP90.3 / YFN-AtRPAP3

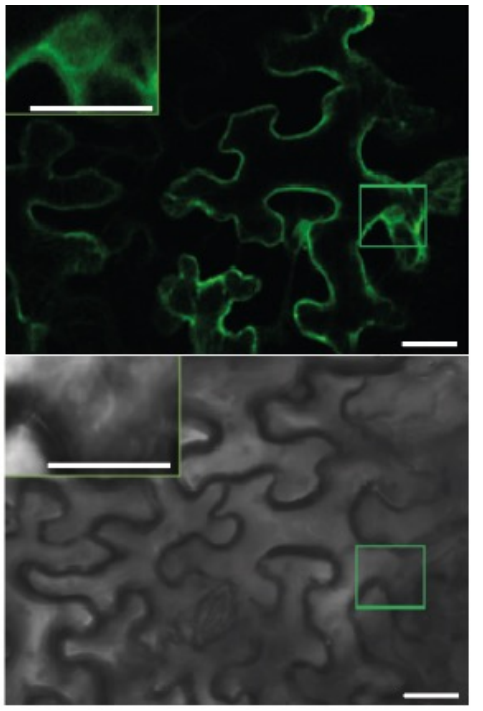

YFC-BBX24 / YFN-AtRPAP3

YFC-AtRuvBL2a / YFN-JAZ3

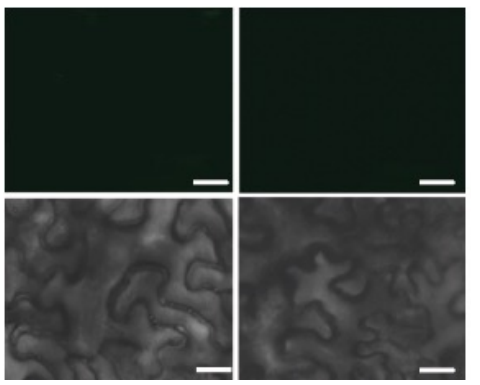

YFC-BBX24 / YFN-AtRPAP3

YFC-AtHSP90.3 / YFN-JAZ3

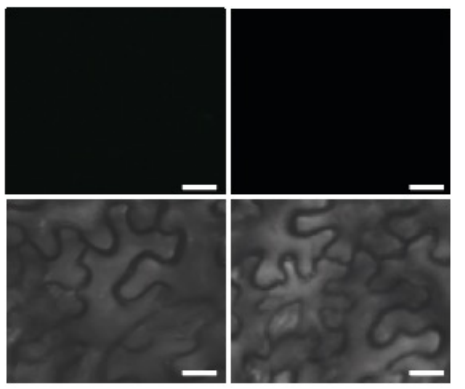

A

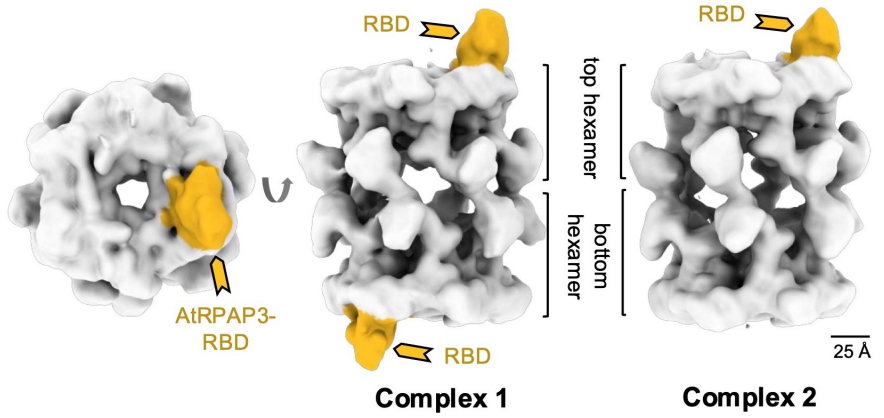


B

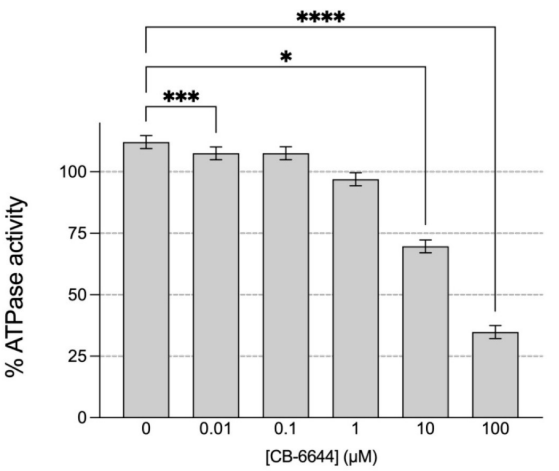


C

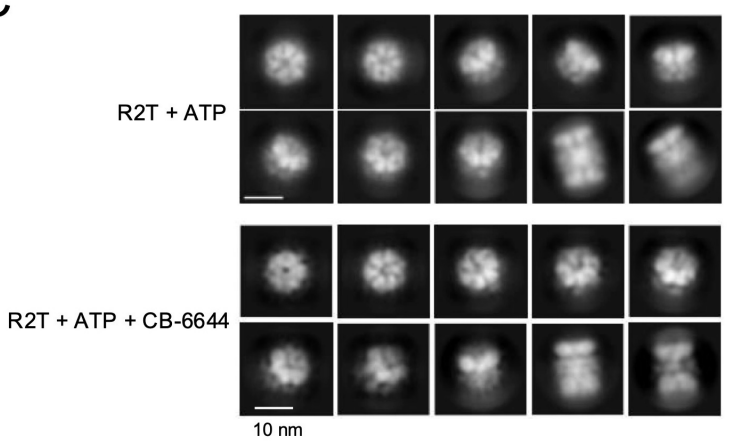


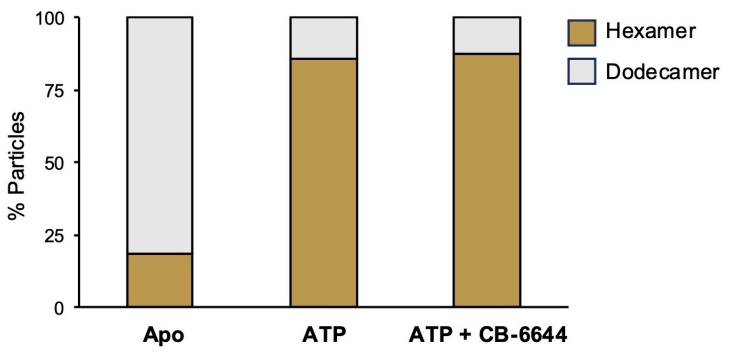


D

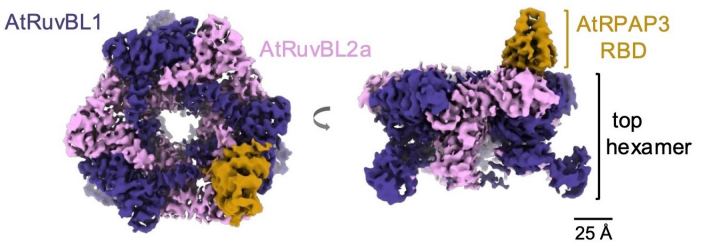


E

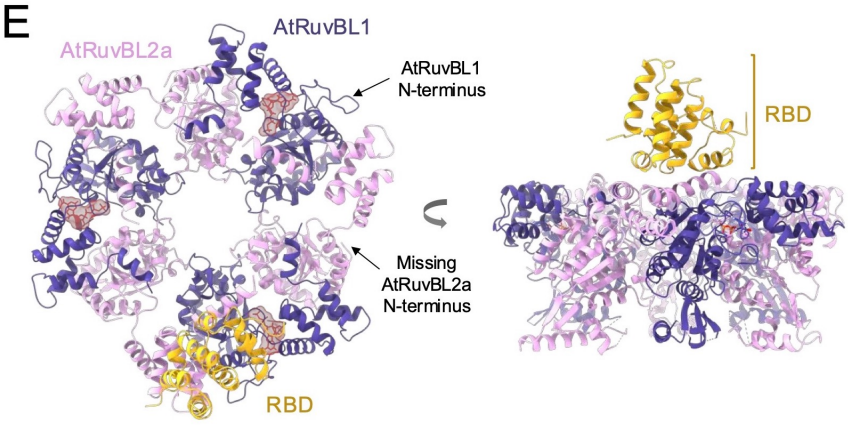


F

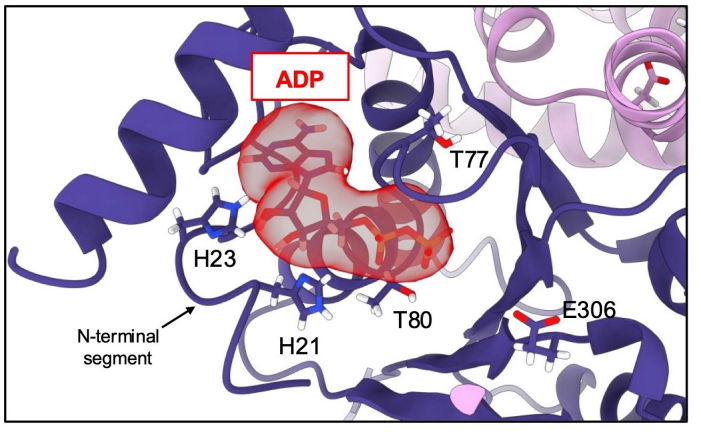


AtRuvBL1

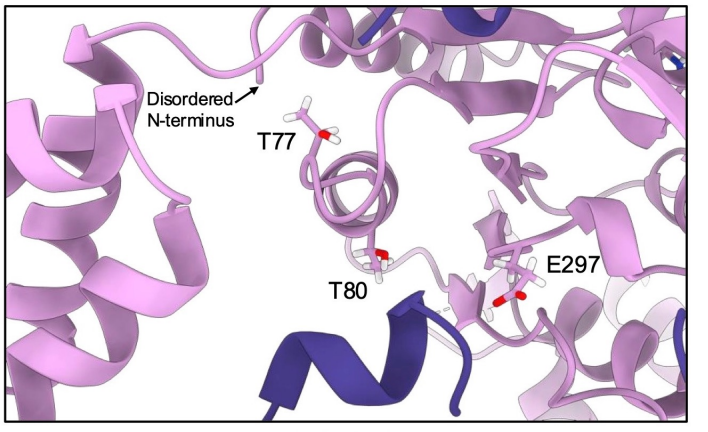


AtRuvBL2a

A

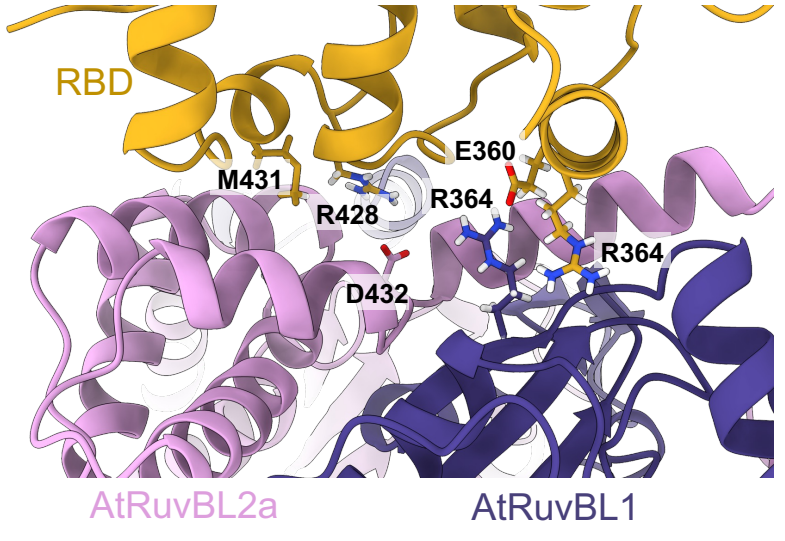
RBD
M431
E360
R428
R364
R364
D432
AtRuvBL2a
AtRuvBL1

B

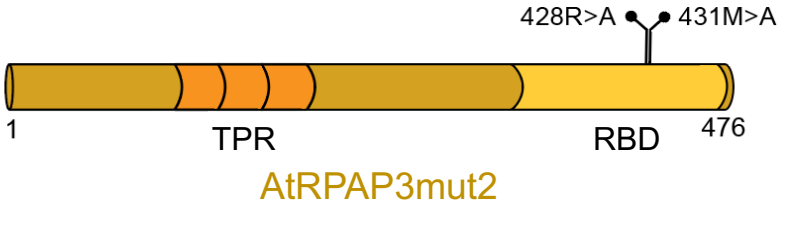
428R>A
431M>A
1
TPR
RBD
476
AtRPAP3mut2

C

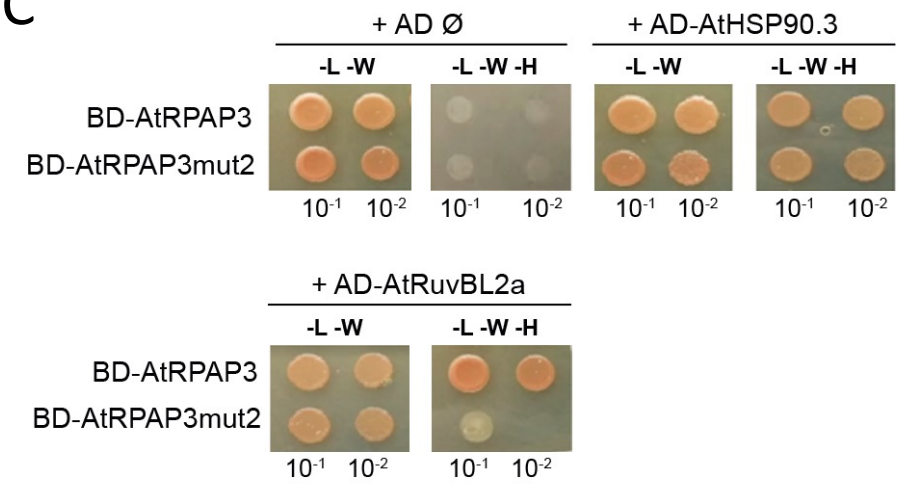
+ AD Ø
+ AD-AtHSP90.3
-L -W
-L -W -H
-L -W
-L -W -H
BD-AtRPAP3
BD-AtRPAP3mut2
10-1 10-2 10-1 10-2
10-1 10-2 10-1 10-2
+ AD-AtRuvBL2a
-L -W
-L -W -H
BD-AtRPAP3
BD-AtRPAP3mut2
10-1 10-2 10-1 10-2

D

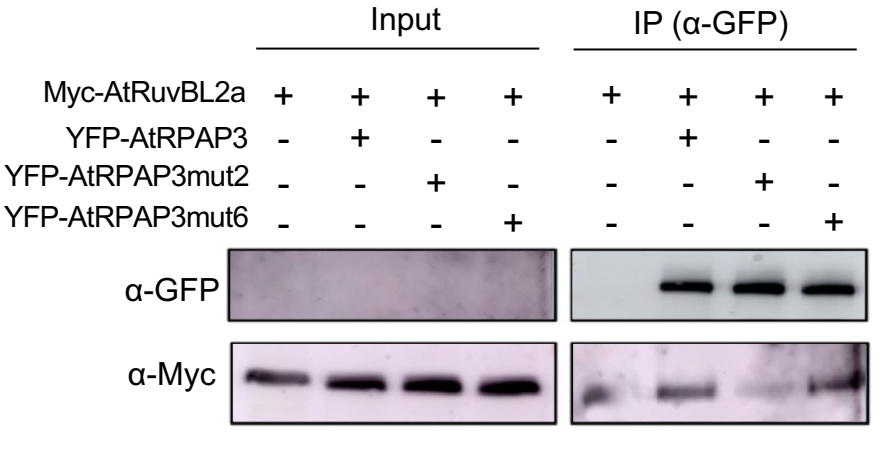
Input
IP (α-GFP)
Myc-AtRuvBL2a + + + + + + + +
YFP-AtRPAP3 - + - - - + - -
YFP-AtRPAP3mut2 - - + - - - + -
YFP-AtRPAP3mut6 - - - + - - - +
α-GFP
α-Myc

A

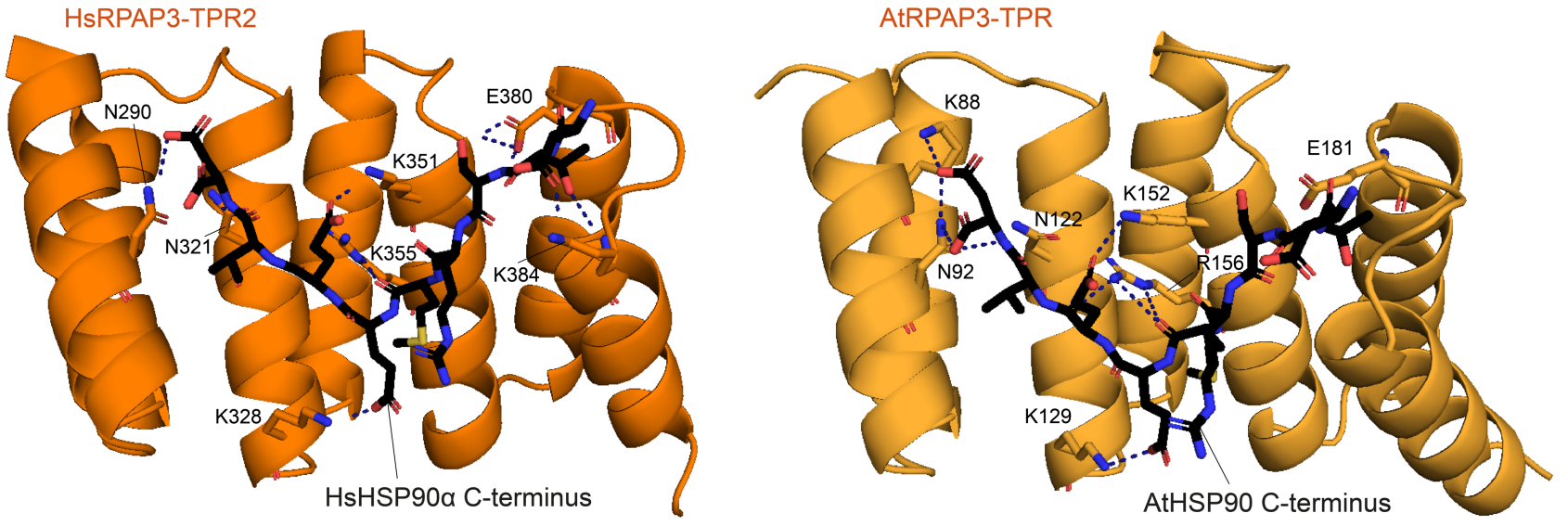
HsRPAP3-TPR2
N290
E380
K351
N321
K355
K384
K328
HsHSP90α C-terminus
AtRPAP3-TPR
K88
E181
K152
N122
N92
R156
K129
AtHSP90 C-terminus

B

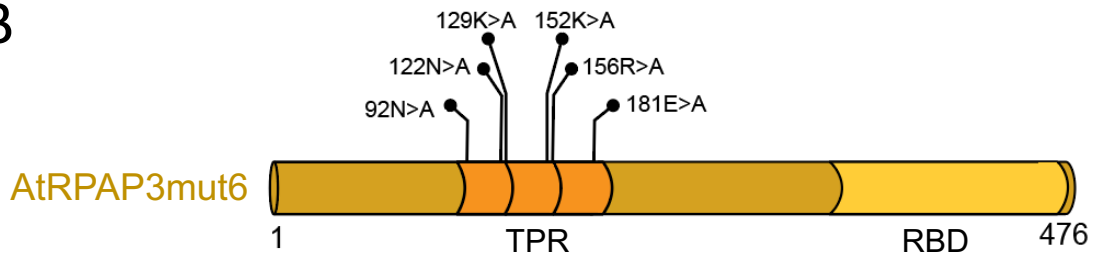
129K>A
152K>A
122N>A
156R>A
92N>A
181E>A
AtRPAP3mut6
1
TPR
RBD
476

C

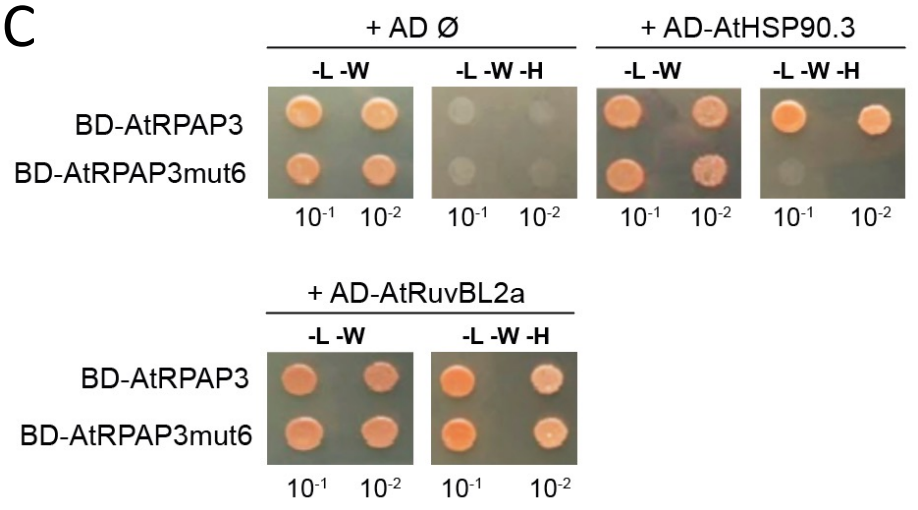
+ AD Ø
+ AD-AtHSP90.3
-L -W
-L -W -H
BD-AtRPAP3
BD-AtRPAP3mut6
10-1 10-2
+ AD-AtRuvBL2a

D

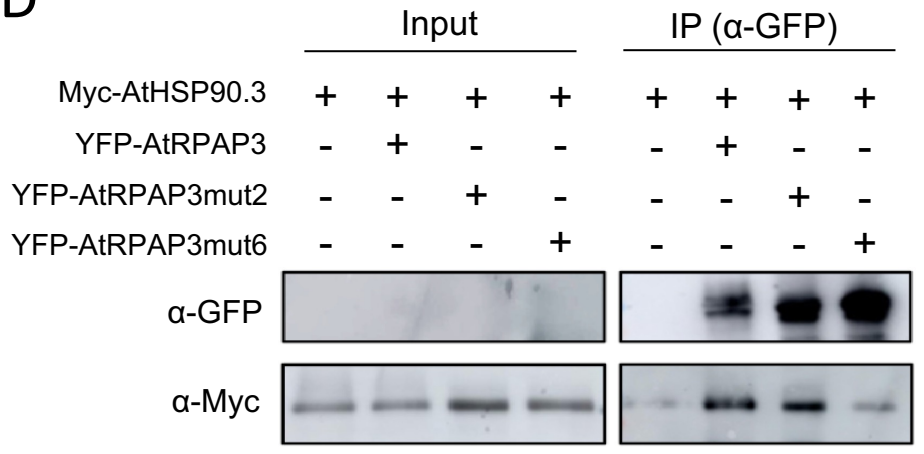
Input
IP (α-GFP)
Myc-AtHSP90.3
YFP-AtRPAP3
YFP-AtRPAP3mut2
YFP-AtRPAP3mut6
α-GFP
α-Myc

A

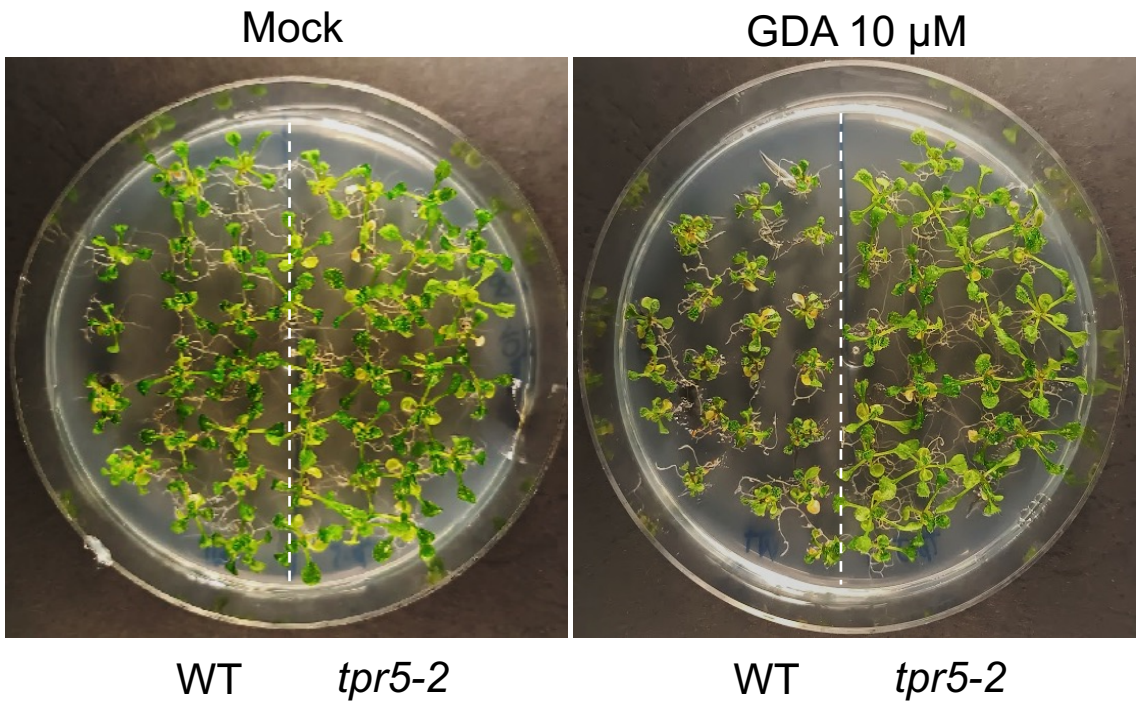
Mock
GDA 10 μM
WT
tpr5-2
WT
tpr5-2

B

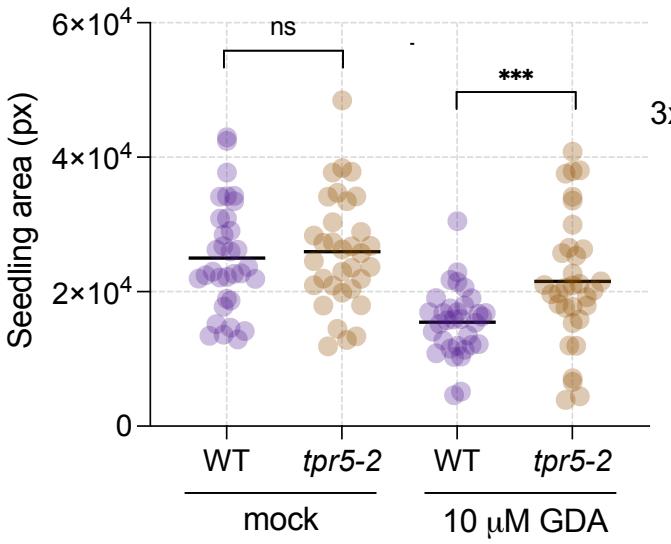
Seedling area (px)
6×10^4
4×10^4
2×10^4
0
ns
***
WT
tpr5-2
WT
tpr5-2
mock
10 μM GDA

C

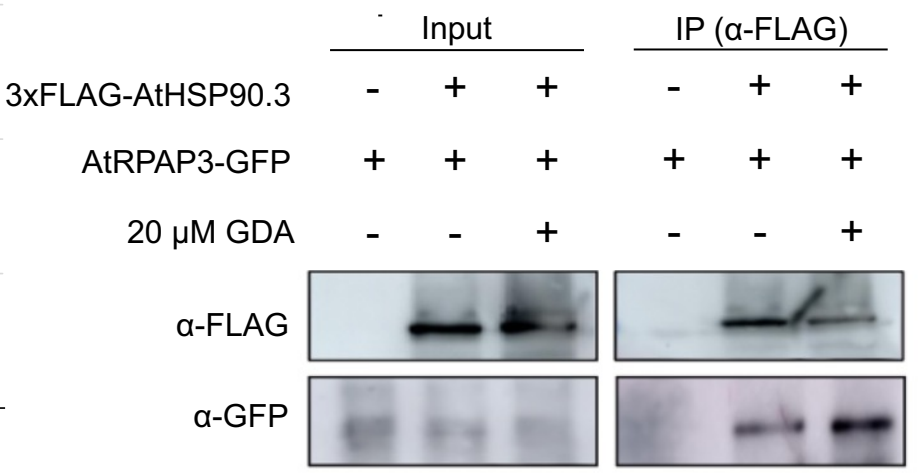
Input
IP (α-FLAG)
3xFLAG-AtHSP90.3
AtRPAP3-GFP
20 μM GDA
α-FLAG
α-GFP

| | | Peptides | | | |
|---|---|---|---|---|---|
| | AGI Code | R1 | R2 | Ranking | Bait groups |
| **PFD6** | AT1G29990 | 669 | 697 | 1 | 0 |
| **PFD3** | AT5G49510 | 498 | 530 | 2 | 0 |
| **PFD2** | AT3G22480 | 437 | 491 | 3 | 0 |
| **PFD5** | AT5G23290 | 205 | 228 | 4 | 0 |
| **PFD4** | AT1G08780 | 121 | 130 | 7 | 0 |
| **PFD1** | AT2G07340 | 90 | 107 | 8 | 0 |

**Figure S1. Table showing the subunits of the canonical PFD complex identified by TAP-MS using GS$^{rhino}$-PFD6 as bait, related to Table 1**. The total number of peptides is indicated for each replicate (R). Ranking refers to the position of each protein in the filtered list of 50 identified proteins, based on the average number of peptides. Bait groups referes to the number of bait groups (out of 62) in which the protein appears as non-specific (see STAR METHODS for details).

A

| | | Peptides | | | |
|---|---|---|---|---|---|
| | AGI Code | R1 | R2 | Ranking | Bait groups |
| **NRPB5A** | AT3G22320 | 18 | 15 | 16 | 0 |
| **NRPC1** | AT5G60040 | 19 | 13 | 17 | 0 |
| **NRPB5C** | AT5G57980 | 12 | 14 | 18 | 0 |
| **NRPB8B** | AT3G59600 | 4 | 3 | 29 | 0 |

B

| | | $GS^{rhino}$-AtRPAP3 | | | $GS^{rhino}$ | | |
|---|---|---|---|---|---|---|---|
| | | Peptides/PSM | | | Peptides/PSM | | |
| | AGI Code | R1 | R2 | R3 | R1 | R2 | Ranking |
| ***RNA polymerase subunits*** | | | | | | | |
| **NRPC1** | AT5G60040 | 48 / 63 | 23 / 28 | 3 / 3 | 0 / 0 | 0 / 0 | 6 |
| **NRPA1** | AT3G57660 | 15 / 17 | 18 / 19 | 0 / 0 | 0 / 0 | 0 / 0 | 28 |
| **NRPB3** | AT2G15430 | 7 / 9 | 7 / 9 | 3 / 3 | 1 / 1 | 1 / 1 | 66 |
| **NRPB5C** | AT5G57980 | 4 / 0 | 9 / 13 | 4 / 5 | 0 / 0 | 0 / 0 | 70 |
| **NRPB1** | AT4G35800 | 8 / 9 | 7 / 7 | 1 / 1 | 0 / 0 | 0 / 0 | 72 |
| ***Adapters*** | | | | | | | |
| **TELO2** | AT3G48470 | 11 / 11 | 10 / 13 | 4 / 5 | 0 / 0 | 0 / 0 | 36 |
| **TTI2** | AT1G79190 | 12 / 15 | 7 / 8 | 2 / 2 | 0 / 0 | 0 / 0 | 50 |
| **TTI1** | AT2G39910 | 6 / 7 | 8 / 9 | 1 / 1 | 0 / 0 | 0 / 0 | 81 |
| **ZNHIT2** | AT5G63830 | 0 / 0 | 10 / 13 | 2 / 2 | 0 / 0 | 0 / 0 | 124 |

**Figure S2. Known clients and adaptors of the R2T complex identified in the proteomics analyses, related to Table 1 and Table 2.** (A) Subunits of nuclear RNA polymerases identified by TAP-MS using $GS^{rhino}$-PFD6 as bait. The number of peptides for each protein identified in each replicate (R) is shown. Ranking refers to the position of each protein in the filtered list of 50 identified proteins, based on the average number of peptides. Bait groups refers to the number of bait groups (out of 62) in which the protein appears as non-specific (see STAR METHODS for details). (B) Subunits of nuclear RNA polymerases and adapters of R2T identified by AP-MS using $GS^{rhino}$-AtRPAP3 as bait. The number of peptides/peptide spectrum matches (PSM) for each protein identified in each replicate (R) is shown. Ranking refers to the position of each protein in the filtered list of 223 identified proteins, based on the average number of peptides.

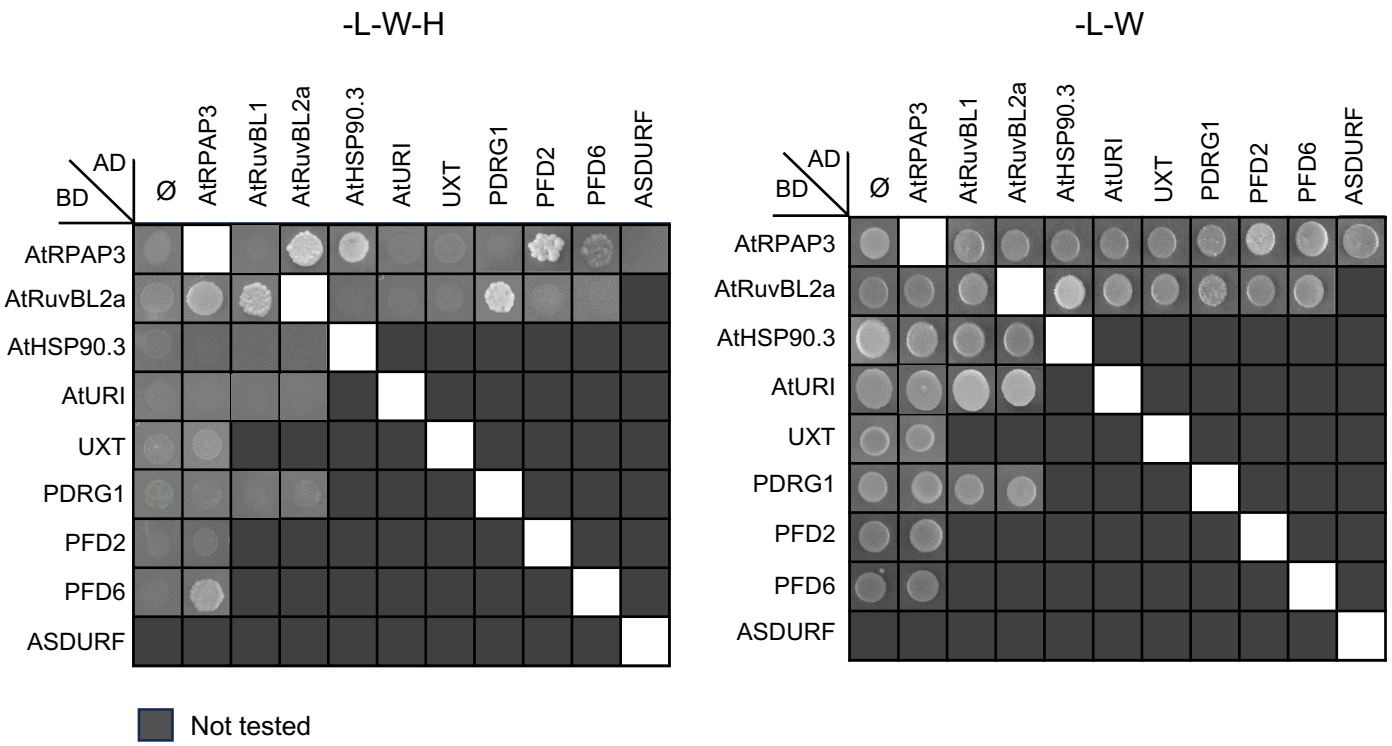


**Figure S3. Drop assay showing the interactions between subunits of R2T and PFDL complexes by Y2H, related to Figure 2.** L, leucine; W, tryptophan; H, histidine.

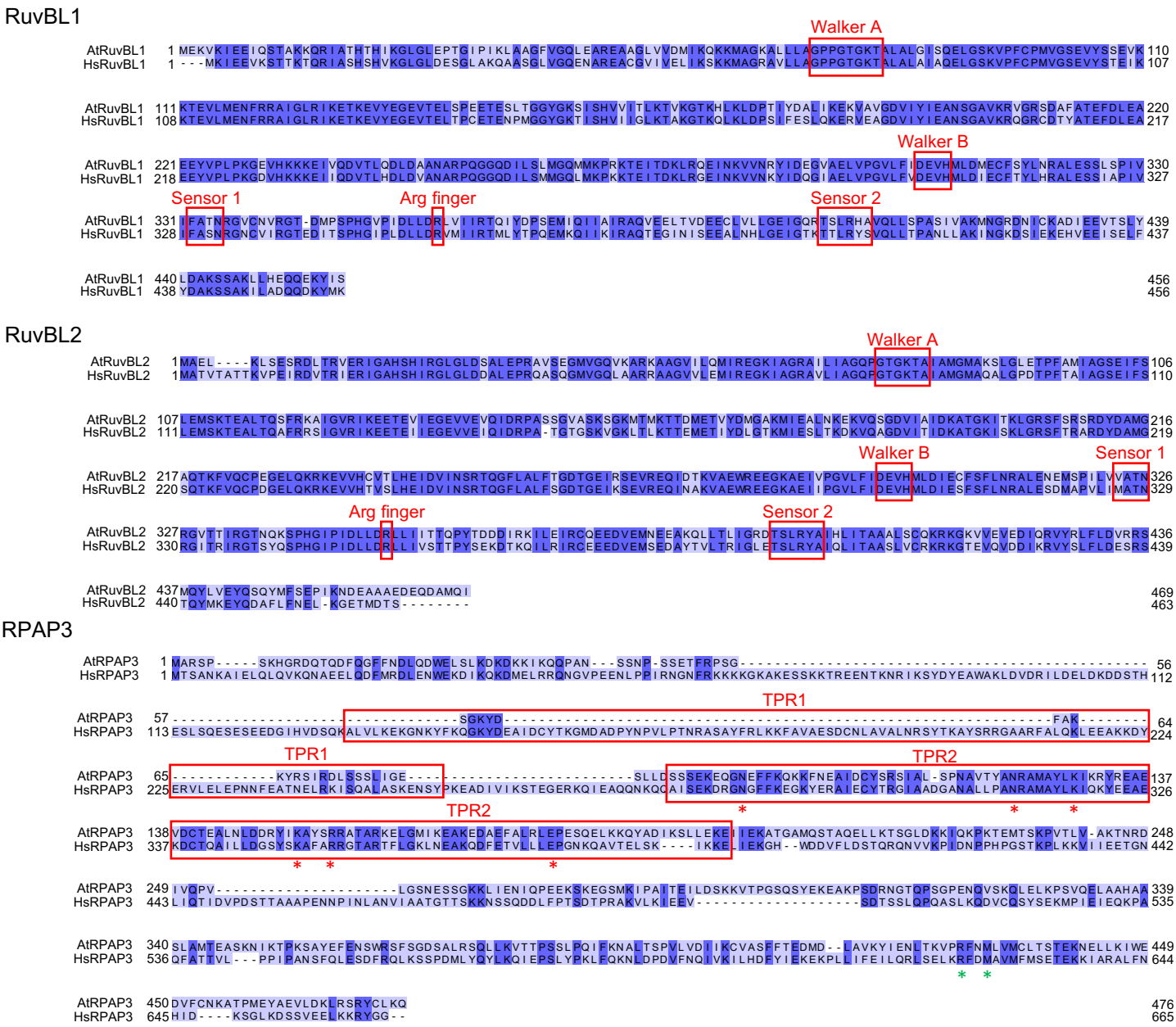


**Figure S4. Sequence alignment of RuvBL1, RuvBL2 and RPAP3 from *Homo sapiens* (Hs) and *Arabidopsis* (At), related to Figures 6 and 7.** The *Arabidopsis* RuvBL2 is AtRuvBL2a. Catalytic residues of RuvBL1 and RuvBL2 and the TPR domains of RPAP3 are indicated. Conserved amino acids (dark blue) were calculated with JALVIEW from the aligned sequences. Green asterisks mark the residues involved in the interaction between AtRPAP3 RBD and AtRuvBL2a. Red asterisks mark the residues involved in the interaction between RPAP3 and HSP90.

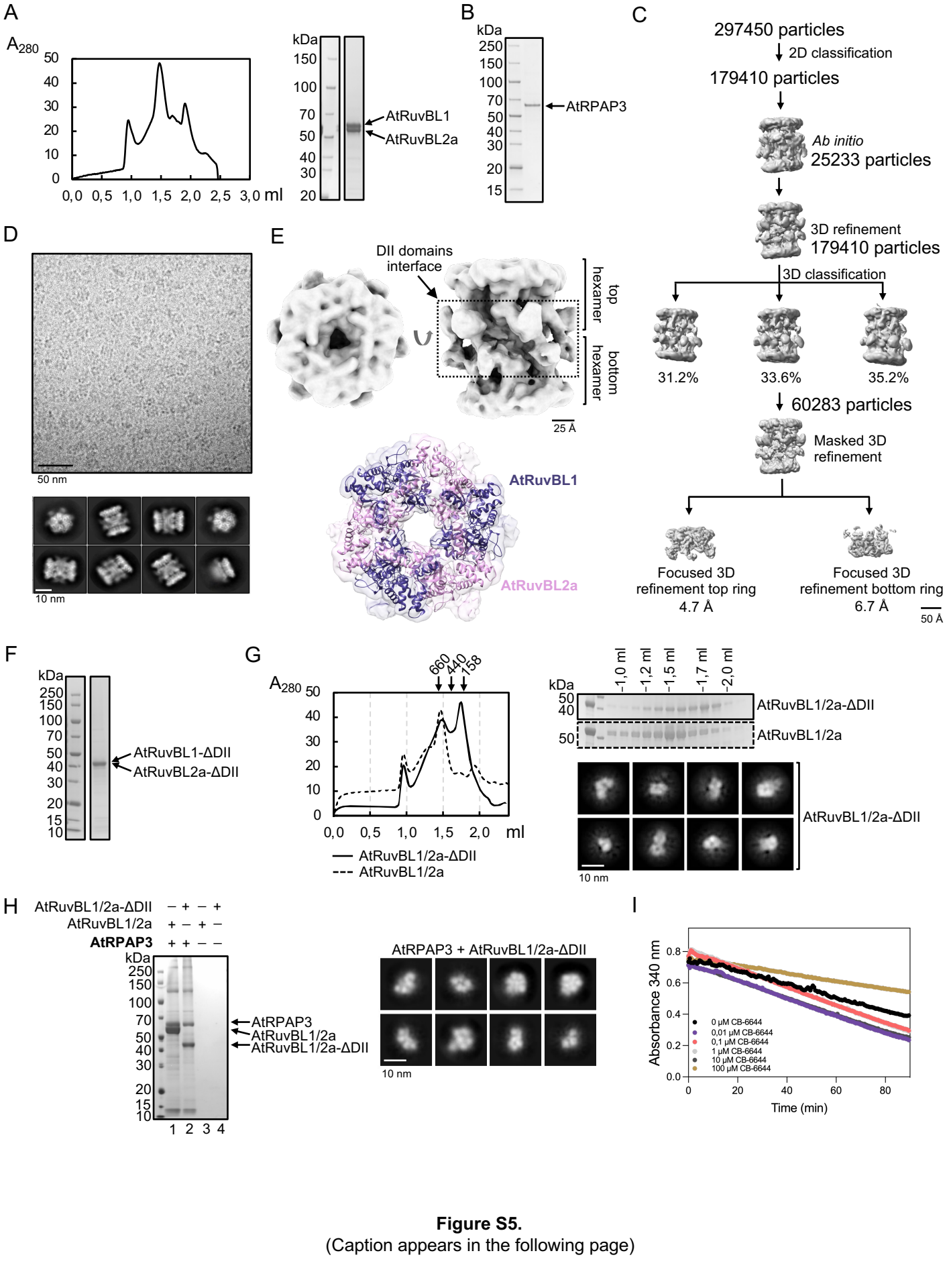


**Figure S5.**
(Caption appears in the following page)

**Figure S5. Structural characterization of the AtRuvBL1-AtRuvBL2a complex, related to Figures 3 and 5.** (A) Size exclusion chromatography (SEC) was used as the final purification step for the recombinant AtRuvBL1-AtRuvBL2a. Coomassie-stained SDS-PAGE shows the peak fraction from the chromatography used for structural experiments and ATPase activity assays. (B) Coomassie-stained SDS-PAGE of purified recombinant AtRPAP3 used in the ATPase activity assay of AtRuvBL1-AtRuvBL2a. (C) Image processing workflow for the cryo-EM images of the AtRuvBL1-AtRuvBL2a complex. Scale bar: 50 Å. (D) Representative cryo-EM micrograph (top) and 2D averages (bottom) of AtRuvBL1-AtRuvBL2a. (E) Cryo-EM 3D reconstruction of the dodecameric AtRuvBL1-AtRuvBL2a complex, highlighting the top and bottom hetero-hexameric modules and the interaction surface formed by DII domains. Bottom panel shows a top view of the complex with the atomic model of the human homologue rigid body fitted in the cryo-EM density (PDB 2XSZ). Scale bars are indicated. (F) Purification of the AtRuvBL1-ΔDII-AtRuvBL2a-ΔDII deletion mutant complex. Coomassie-stained SDS-PAGE of purified recombinant AtRuvBL1-ΔDII-AtRuvBL2a-ΔDII. Since the bands for the two proteins were not distinguishable, the presence of both proteins was confirmed by mass spectrometry. (G) SEC fractionation of mutant AtRuvBL1-ΔDII-AtRuvBL2a-ΔDII (solid line) and wild-type AtRuvBL1-AtRuvBL2a (dash line) complexes. Elution points for some molecular weight standards (kDa) are indicated above with arrows. The right upper panel shows SDS-PAGE of fractions from the chromatography, indicating the elution volumen. The right bottom panel shows reference-free 2D class averages of negative-stain EM images for the mutant complex after SEC, where neither hexameric nor dodecameric complexes were identified. Scale bar: 10 nm. (H) SDS-PAGE of the elution from a pull-down experiment testing the interaction of AtRPAP3 (bait, in bold) with AtRuvBL1-AtRuvBL2a (lane 1) or AtRuvBL1-ΔDII-AtRuvBL2a-ΔDII (lane 2). Control experiments with only the prey proteins are also shown (lanes 3 and 4). Bottom panel shows reference-free 2D averages of negative-stain EM images from the co-elution of AtRPAP3 and AtRuvBL1-ΔDII-AtRuvBL2a-ΔDII. The characteristic oligomers of the complex were not observed for this specimen, similar to the AtRuvBL1-ΔDII-AtRuvBL2a-ΔDII sample analyzed in (F). (I) Representative time course curves of ATP turn over by AtRuvBL1-AtRuvBL2a (black line), and after incubation with increasing concentrations of CB-6644 (0.01, 0.1, 1, 10, and 100 μM; purple, red, light grey, dark grey, and gold lines, respectively). Slopes from the curves were used to calculate the rate of ATP consumption shown in Figure 5B.

A

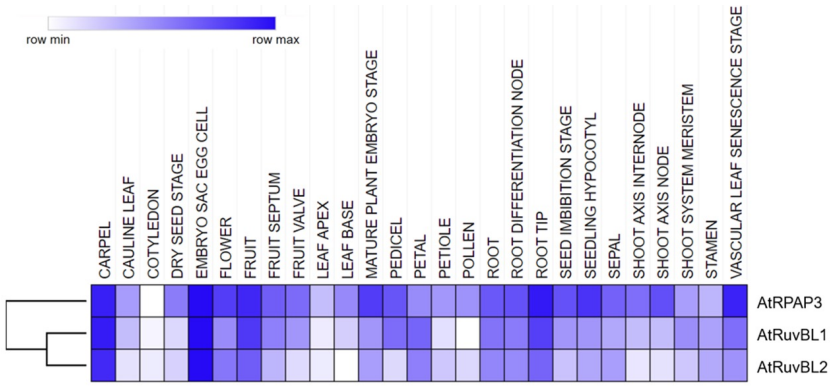


B

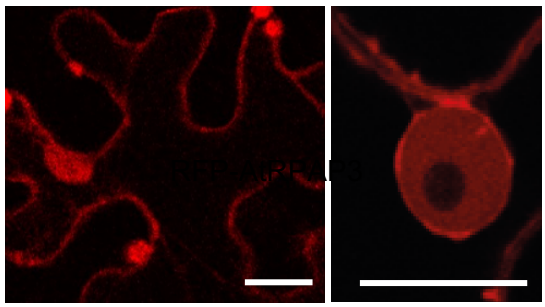

**Figure S6. The R2T subunits exhibit similar accumulation patterns, related to Figure 4.** (A) Normalized protein accumulation in various *Arabidopsis* organs using ProteomicsDB. AtRuvBL2 refers to AtRuvBL2a. (B) Nuclear and cytoplasmic localization of AtRPAP3, fused to RFP tag, in *N. Benthamina* leaves (Scale bar: 10μm).

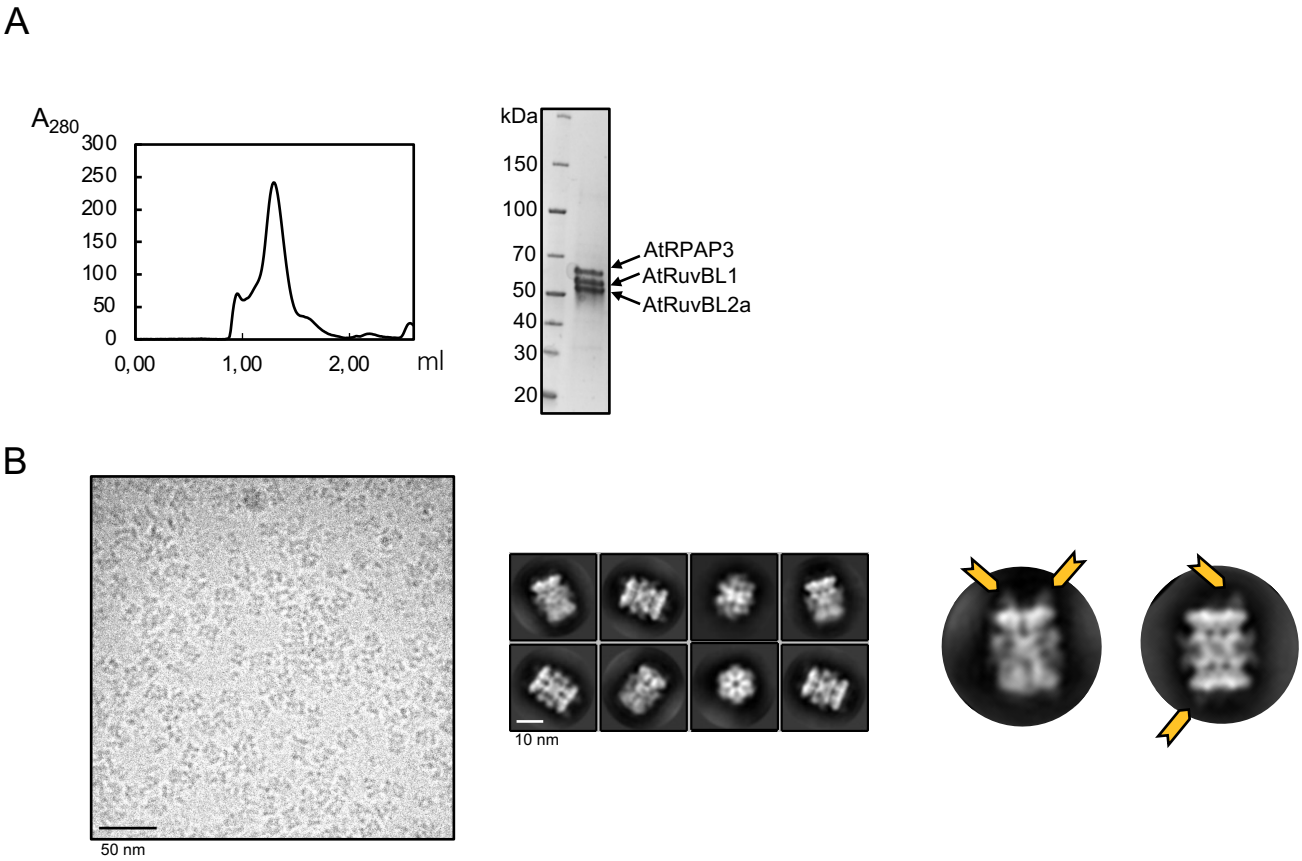


**Figure S7. Purification and preliminary structural characterization of the *Arabidopsis* R2T complex, related to Figure 5.** (A) AtRuvBL1, AtRuvBL2a and AtRPAP3 where co-expressed to favor complex formation *in vivo*. Chromatogram shows the size exclusion purification of ther R2T complex. Coomassie-stained SDS-PAGE shows the peak fraction from the chromatography used cryo-EM experiments. (B) Cryo-EM field (left) and 2D averages (middle) of R2T. Scale bars are indicated. The complex displayed a dodecameric architecture similar to AtRuvBL1-AtRuvBL2a with extra densities attached to the AAA+ face of the hexameric rings (labeled with yellow arrows in the right inserts).

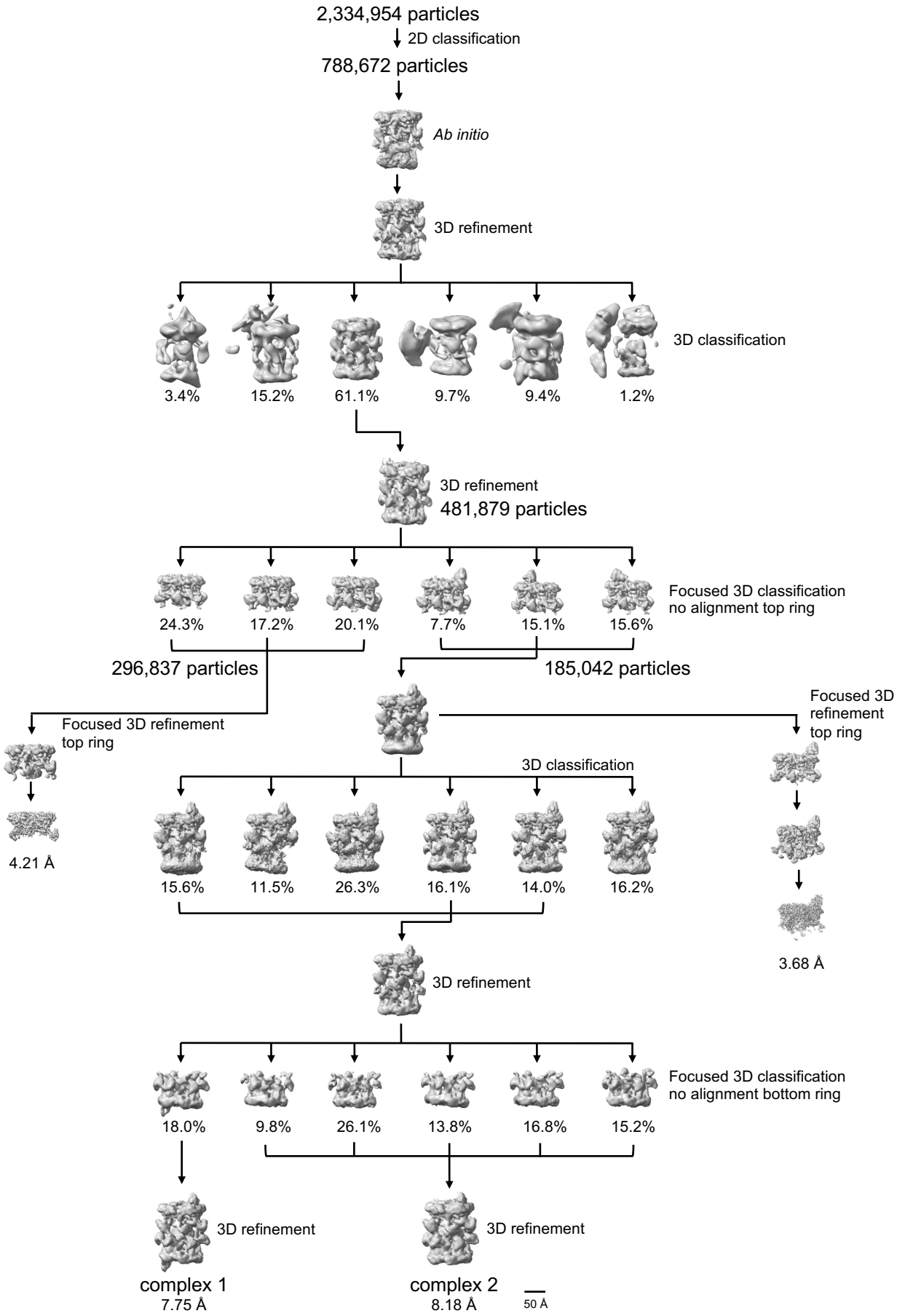


**Figure S8**. **Image processing workflow of the cryo-EM images of the R2T complex, related to Figure 5.** Scale bar represents 50 Å.

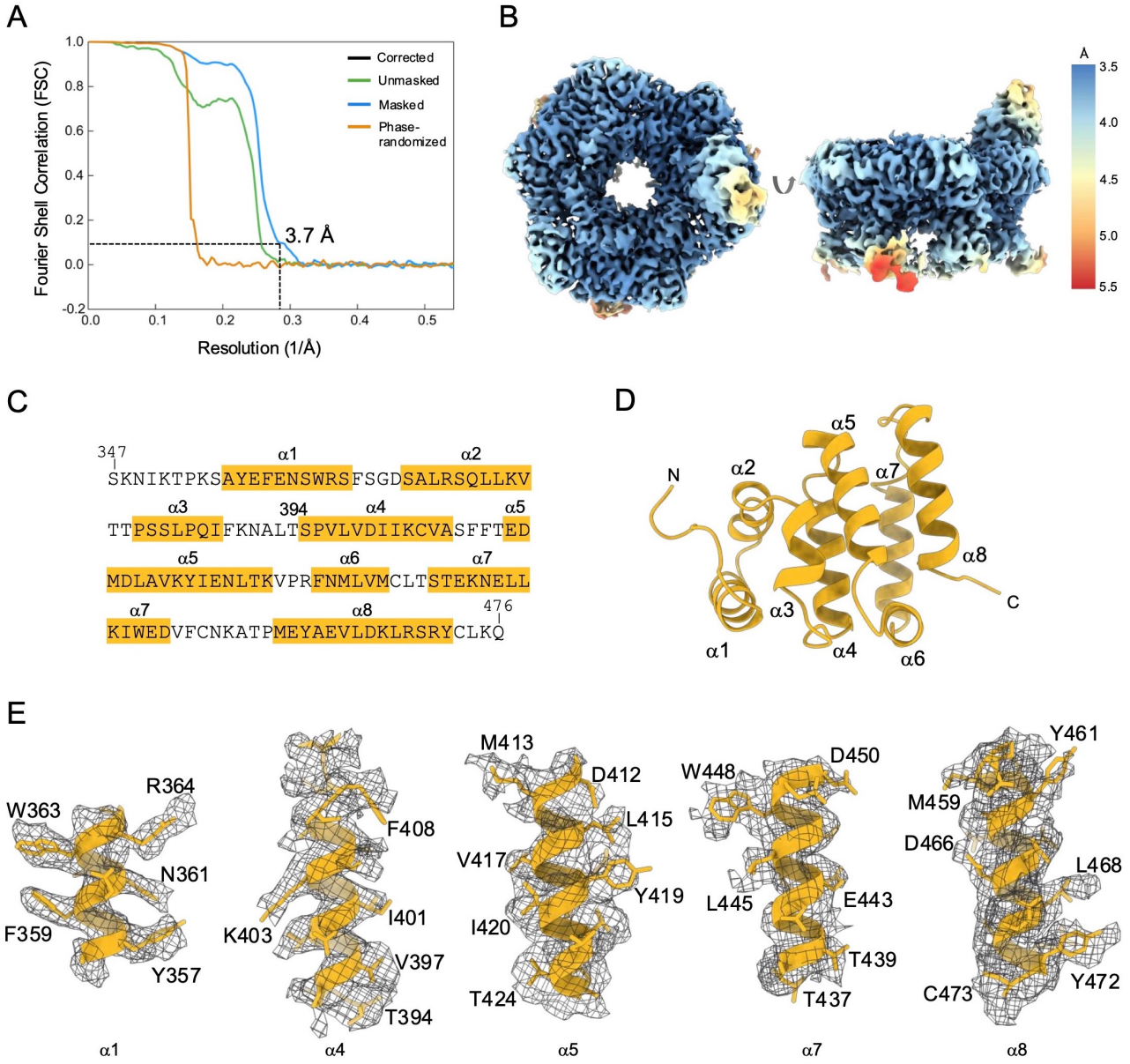


**Figure S9. Resolution estimation of the cryo-EM for the R2T top ring, related to Figures 5 and 6.** (A) Fourier Shell Correlation (FSC) curves for the R2T core complex obtained by focused refinement of the top ring in the dodecameric structure. (B) Local resolution estimates for the R2T top ring complex as provided by RELION. Bottom and side views of the map are shown using the color scale shown on the right. (C) Sequence of AtRPAP3 RBD domain highlighting the α-helices in orange. (D) Ribbon representation of the AtRPAP3 RBD domain from the R2T complex. α-helices 1 to 8 are indicated. (E) Cryo-EM density maps (shown in mesh) for representative regions of the AtRPAP3 RBD domain shown with the atomic model fitted within the cryo-EM density. Several residues are indicated showing the side chains.

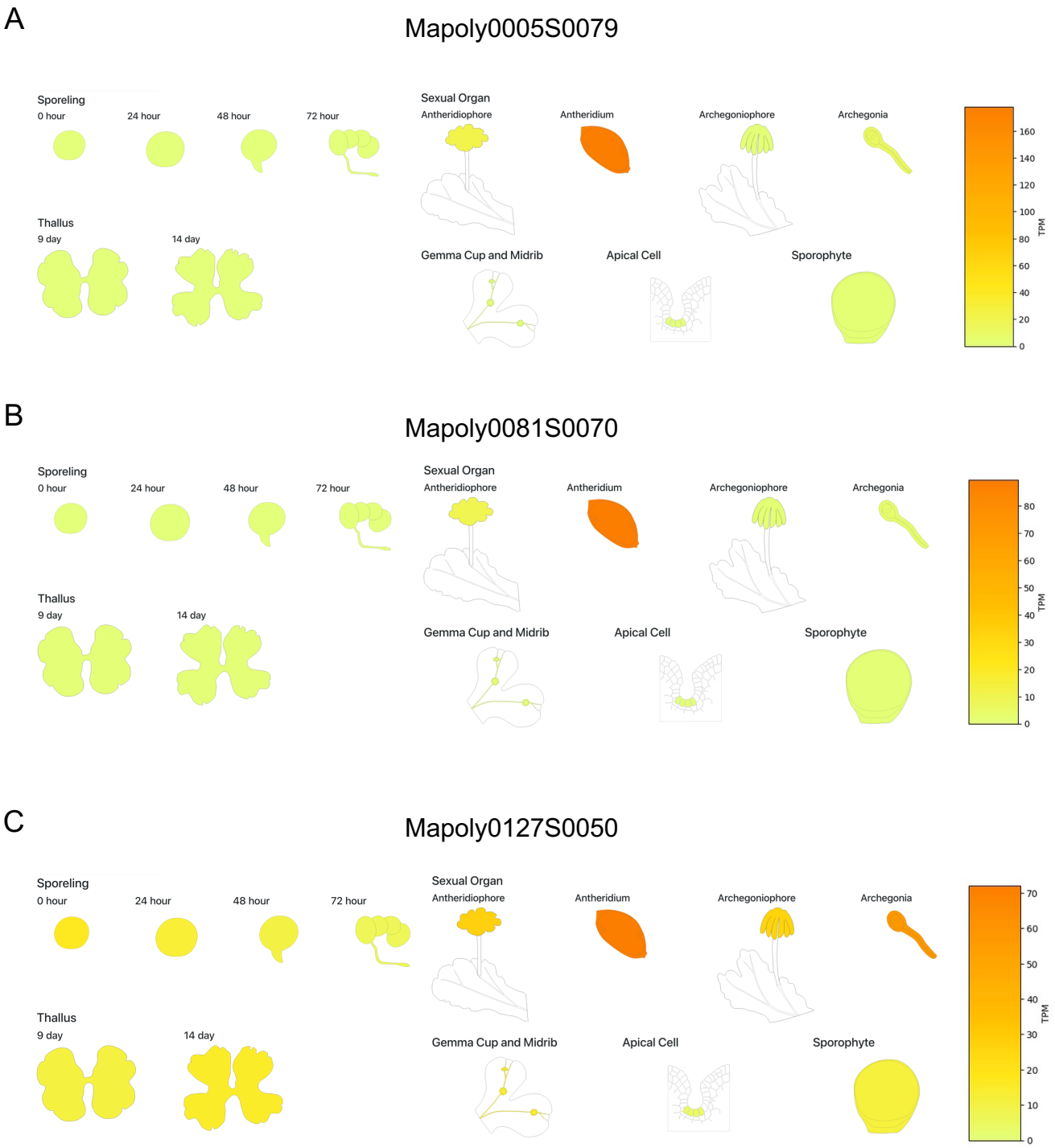


**Figure S10. Tissue-specific expression in *Marchantia polymorpha*, related to Figure 4.** (A, B) Chromatic expression images of the two *Marchantia* genes encoding proteins with a PIH domain. (C) Chromatic expression images of the only gene of *Marchantia* encoding a protein with a TPR domain and an RBD found in RPAP3. Expression levels are shown in TPM in the color-coded bar. The data was obtained using the Expression Database for *Marchantia polymorpha* (https://marchantia.info/mbex/).

**Table S2. Cryo-EM data collection, refinement, and validation statistics, related to Figures 5, 6, and STAR Methods.**

| Structure | *Arabidopsis* R2T complex (EMD-19894) (PDB ID 9EQ2) |
|---|---|
| **Data collection and processing** | |
| Microscope | Titan Krios |
| Detector | Falcon 4i |
| Nominal magnification | 130,000 |
| Voltage (kV) | 300 |
| Electron exposure ($e^-/Å^2$) | 50.12 (50 fractions) |
| Defocus range (μm) | -1.5 to -3.0 |
| Pixel size (Å) | 0.921 |
| Symmetry imposed | C1 |
| Initial particle images (no.) | 2,334,954 |
| Final particle images (no.) | 185,042 |
| Map resolution (Å) | 3.68 |
| FSC threshold | 0.143 |
| Map resolution range (Å) | 3.5 – 5-5 |
| **Refinement** | |
| Initial model used | AlphaFold |
| Map sharpening B factor ($Å^2$) | -128.2 |
| **Model composition** | |
| Non-hydrogen atoms | 14628 |
| Protein residues | 1876 |
| Nucleotide residues | 0 |
| Ligands | ADP:3 |
| **R.m.s. deviations** | |
| Bond lengths (Å) | 0.007 |
| Bond angles (°) | 1.030 |
| **Validation** | |
| MolProbity score | 1.22 |
| Clashscore | 2.79 |
| Rotamers outliers (%) | 0.25 |
| **Ramachandran (%)** | |
| Favored | 97.17 |
| Allowed | 2.83 |
| Disallowed | 0.00 |
| **Model vs Data** | |
| CC volume | 0.72 |

**Table S3. Oligonucleotides used in this work, related to STAR Methods.**

| *Cloning of CDSs (Gateway)* | |
|---|---|
| AtRPAP3_attB1_Fw | GGGGACAAGTTTGTACAAAAAAGCAGGCTTCATGGCTAGGTCACCGAGCAA |
| AtRPAP3_attB2_Rv | GGGGACCACTTTGTACAAGAAAGCTGGGTTTACTGTTTAAGGCAGTATC |
| AtRPAP3_attB2_noSTOP_Rv | GGGGACCACTTTGTACAAGAAAGCTGGGTCCTGTTTAAGGCAGTATCTTGAC |
| AtRuvBL1_attB1_Fw | GGGGACAAGTTTGTACAAAAAAGCAGGCTTCATGGAGAAAGTAAAGATTGA |
| AtRuvBL1_attB2_Rv | GGGGACCACTTTGTACAAGAAAGCTGGGTCTGAGATGTATTTTTCTTGTT |
| AtRuvBL2a_attB1_Fw | GGGGACAAGTTTGTACAAAAAAGCAGGCTTCATGGCGGAACTAAAGCTATC |
| AtRuvBL2a_attB1_Fw | GGGGACCACTTTGTACAAGAAAGCTGGGTCGATCTGCATAGCATCTTGTT |
| AtRuvBL1_deltaDII_Fw | GGAAGGACCTCCAGGTATAGTGCAGGATGTCACACTCCAAG |
| AtRuvBL1_deltaDII_Rv | CTATACCTGGAGGTCCTTCCTTGATACGTAGACCAATGGCA |
| AtRuvBL2a_deltaDII_Fw | AGAAGGACCTCCAGGTGTTGTACATTGTGTCACTCTTCACG |
| AtRuvBL2a_deltaDII_Rv | CAACACCTGGAGGTCCTTCTTTGATCCTAACACCAATCGCT |
| AtRPAP3mut2_int_Fw | ACAAAGGTTCCTGCATTCAACGCACTCGTCATGTGCC |
| AtRPAP3mut2_int_Rv | GGCACATGACGAGTGCGTTGAATGCAGGAACCTTTGT |
| *Cloning in bacterial expression plasmids* | |
| pET15b_AtRuvBL1_BamHI_Fw | ATATGCTCGAGGATCCAATGGAGAAAGTAAAGATTGAAGAAATTCAGTCCA |
| pET15b_AtRuvBL1_BamHI_Rv | GTTAGCAGCCGGATCCTCATGAGATGTATTTTTCTTGTTGCTCATGC |
| pCDFDuet_AtRuvBL2a_KpnI_Fw | CGGGGTACCATGGCGGAACTAAAGCTAT |
| pCDFDuet_AtRuvBL2a_KpnI_Rv | CGGGGTACCTCAGATCTGCATAGCATCTTG |
| pRSFDuet_1_Cons_TEV_AtRPAP3_FW | GAGAGAATCTTTATTTTCAGGGCATGGCTAGGTCACCGAGCAAACACG |
| pRSFDuet_2_AtRPAP3_cons_3C_RV | TGGAACAGCACCTCCAGCTGTTTAAGGCAGTATCTTGACCTTAGTTTGTC |
| pRSFDuet_Vector_Cons_Fw | CTGGAGGTGCTGTTCCAGGGACCT |
| pRSFDuet_Vector_Cons_Rv | GCCCTGAAAATAAAGATTCTCTCCGCC |
| *Preparing the AtHSP90.3:6xHis-TEV-3xFLAG-AtHSP90.3 construct* | |
| -1141_TSS_AtHSP90.3_Fw | GGGACAAGTTTGTACAAAAAAGCAGGCTTCGGGGGAAAAGTGTGTAATATATAGGGGATG |
| AtHSP90.3_genomic_Rv | GGGGACCACTTTGTACAAGAAAGCTGGGTCTTAGTCAACTTCCTCCATCTTGCT |
| NcoI_6xHis-3xFlag_Fw | CATGCCATGGGTCATCACCATCACC |
| NcoI_6xHis-3xFlag_Rv | CATGCCATGGTTCCTTTGTCGTCA |
| AtHSP90-3flag_NcoI_Fw | CGATCAACGACCATGGGTCATCACCATCACCATCACGATTATGAT |
| AtHSP90-3flag_NcoI_Rv | TCCGTCGCGACCATGGTTCCTTTGTCGTCATCATCTTTATAGTCTTTATC |